Global compositional cartography of Pluto from intensity-based registration of LEISA data

L.R. R Gabasova, B Schmitt, W. Grundy, T. Bertrand, C.B. B Olkin, J.R. R Spencer, L.A. A Young, K. Ennico, H.A. A Weaver, S.A. A Stern

Global compositional cartography of Pluto from intensity-based registration of LEISA data

L. R. Gabasova[a], B. Schmitt[a], W. Grundy[b], T. Bertrand[c], C. B. Olkin[d], J. R. Spencer[d], L. A. Young[d], K. Ennico[c], H. A. Weaver[e], S. A. Stern[c], the New Horizons Composition Team

[a1] *Université Grenoble Alpes, CNRS, IPAG (Grenoble, France)*
[b] *Lowell Observatory (Flagstaff, AZ, USA)*
[c] *NASA Ames Research Center (Mountain View, CA, USA)*
[d] *SwRI (Boulder, CO, USA)*
[e] *JHU-APL (Laurel, MD, USA)*

Abstract

In 2015 the New Horizons spacecraft reached the Pluto system and returned unprecedentedly detailed measurements of its surface properties. These measurements have already been integrated into global reflectance, topography and narrow-band multispectral surface maps. However, analysis of the hyperspectral data from the Ralph/LEISA infrared spectrometer, which lets us analyse the surface composition, has until now been confined to the high-resolution encounter hemisphere of Pluto. We use an innovative technique — intensity-based registration — to co-register this high-resolution data with lower-resolution measurements taken during the spacecraft's approach, and present the first global qualitative composition maps for CH_4, N_2 and H_2O ice, and a tholin-like red material. We compare these maps with the other maps produced for Pluto and study the global extent of the previously-described latitudinal distribution of the surface components, which is relatively longitudinally constant with the exception of Sputnik Planitia. We also correlate these compositional components with geological features and propose physical interpretations, which include: CH_4-ice-rich dissected plateaus in high northern latitudes, CH_4-rich eroded terrain with N_2-rich infill in medium northern latitudes, CH_4-rich bladed terrain in low northern latitudes, and a red material belt overlaying H_2O ice in low southern latitudes.

Keywords: Pluto, surface, Ices, IR spectroscopy, Image processing

1. Introduction

The July 2015 flyby of the Pluto system by the NASA New Horizons mission returned a wealth of data, in particular greatly advancing our knowledge of its surface topography, geology, and composition. Before New Horizons, a first insight into the spatial distribution of Pluto's different surface components had been inferred from the rotational variations in band depths in ground-based near-IR hemispheric observations (Grundy and Buie, 2001;

Email address: leila.gabasova@univ-grenoble-alpes.fr (L. R. Gabasova)

Grundy et al., 2013), coupled with HST low spatial resolution images (Stern et al., 1997; Buie et al., 2010) which allowed for a global map consisting of $\sim 40-55$ resolution elements.

New Horizons, however, was the first to directly map Pluto's composition. The high spatial resolution data (6-7 km/px) is limited to the encounter hemisphere of Pluto, with partial even higher-resolution coverage at 2.7 km/px over about 11% of the surface, but the series of hyperspectral images obtained during the approach phase[1] provided a lower-resolution view of its other hemisphere, facing Charon, allowing for the production of a global mosaic.

The New Horizons instrument collecting surface composition data is the Ralph spectrograph, which consists of two components: the Multispectral Visible Imaging Camera (MVIC) and the Linear Etalon Imaging Spectral Array (LEISA). MVIC has two panchromatic channels and four colour channels, providing overlapping coverage of the 400-975 nm wavelength range and obtaining a maximum spatial resolution of 0.66 km/pixel for the encounter hemisphere as imaged at closest approach. LEISA, although its pixel field-of-view is three times wider than that of MVIC, provides a complete spectrum in the 1.25-2.5 μm range with an average resolving power ($\lambda/\Delta\lambda$) of 240 (Reuter et al., 2008).

Using the high-resolution LEISA observations, Schmitt et al. (2017) gives a comprehensive qualitative analysis of the spatial distribution of the various materials present on the surface of the encounter hemisphere. N_2-rich and CH_4-rich ices are present both separately and mixed together, possibly either as a two-phase system or as stratified phases. N_2-rich ice consists of CO and CH_4 molecules present at low concentration in a ternary molecular mixture with the dominant N_2, according to the phase diagrams. Also present are H_2O ice and a dark red organic material. This analysis is complemented by a first quantitative study using pixel-by-pixel Hapke modelling of the spectra (Protopapa et al., 2017), but both of these studies are restricted to the high-resolution data of the encounter hemisphere.

While global coverage of the illuminated parts of Pluto (excluding the south polar region, currently experiencing continuous polar night) is possible via the lower-resolution approach images, the imprecision in the instrument's pointing information resulted in spatial misregistration between the encounter and approach datasets that reached several native pixels, i.e. up to several degrees of latitude and/or longitude. Additional co-registration work was thus needed before a global mosaic could be created.

Schenk et al. (2018) produced a panchromatic global reflectance map using both the LORRI (Long Range Reconnaissance Imager) framing camera, the instrument with the highest spatial resolution on board New Horizons, and the MVIC panchromatic channels, which were mosaiced together using a network of control points. Subsequently, Earle et al. (2018) co-registered the MVIC colour channel images on the LORRI image and produced a narrow-band (0.89-μm band) methane equivalent width map and a global visible spectral slope map. The high-resolution LEISA data has also been registered to the panchromatic map using feature-based methods. These methods, however, have proven inadequate for registering the LEISA approach imagery, as the imaging distance combined with the larger pixel

[1] See 2.2 for timestamps corresponding to approach vs. encounter phase.

field-of-view of the instrument results in low-resolution imagery without readily identifiable geological feature edges in the Charon-facing hemisphere.

This paper demonstrates a registration method very rarely used in remote sensing and not at all in planetary science — and heretofore largely published as a proof-of-concept (Liang et al., 2014; Okorie and Makrogiannis, 2019) — and presents the first global qualitative presence maps for the major surface components of Pluto, analogous to those in Schmitt et al. (2017) but extended across the full surface, the continuously shaded south hemisphere excepted. There is ongoing work to produce quantitative maps from these datasets with inverse radiative transfer modeling, which will soon be ready for publication.

2. Methods

2.1. Intensity-based registration

Image registration involves transforming one or more source images to match a target image. Image registration methods can be classified into two broad categories: feature-based and intensity-based. Feature-based registration is based on identifying and aligning distinctive features (such as points, lines or contours) in the images, and is the most common type of method used in remote sensing (Zitova and Flusser, 2003). However, it is labour-intensive, as feature mapping frequently needs to be done manually by selecting the anchor points, and its application is limited to datasets in which sharp, easy-to-map features (crater rims, cliffs, faults, etc.) are present and still recognisable in the lowest-resolution image used.

The second type of method, intensity-based registration, involves comparing intensity patterns in the images to be registered. Different metrics can be used to evaluate their similarity, such as cross-correlation, mutual information, or sum of squared intensity differences. Figure 1 shows how a joint histogram may be used to evaluate the misalignment of two images. Intensity-based registration is underused in planetary science, but is a very common tool in medical imagery processing, where it is used for MRI (magnetic resonance imaging) or CT (X-ray computed tomography) scan images (Pluim et al., 2003). This means most toolkits developed for intensity-based registration, such as ITK (Insight Segmentation and Registration Toolkit, Schroeder et al., 2003), are designed around medical uses — but they can be very easily adapted to planetary data (see Liang et al., 2014, for a demonstration of a combined feature- and intensity-based registration technique on Landsat data).

Registration methods may also be categorised according to what kind of transformations they use for aligning the images. The transformation may be global, with operations such as translation, rotation, scaling, and shear affecting the whole image uniformly, or locally, i.e. defined by a warp field whose effect varies across the image. Insofar as this paper is concerned, the errors in registration of the LEISA data are caused by imprecision in the instrument pointing, resulting in an overall shift of the image and possibly a slight rotation. We can therefore restrict ourselves to global transformations applied to the original orthographic projection.

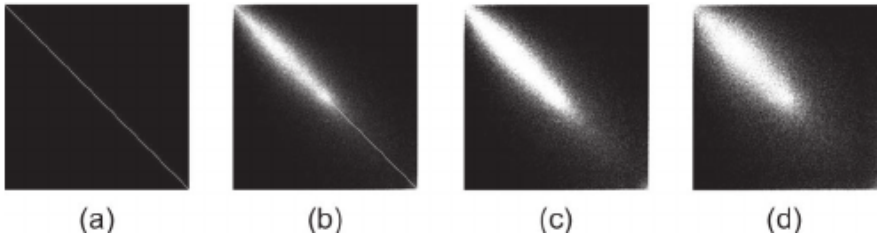

Figure 1: Illustration of the effect of misregistration, showing the joint histogram of a remote-sensed image with itself. In (a) no transformation is performed. In (b), (c), and (d), one image is translated by 0.5, 1, and 2 pixels, respectively (Liang et al., 2014).

2.2. LEISA dataset

During the approach phase each LEISA hyperspectral image fully contains Pluto and is recorded over a short period of time, which means the same transformation matrix will be applicable to all wavelengths of the same hyperspectral image. This lets us calculate the transformation matrix using a spectral subset — one which features large contrasts and clear patterns — and apply it to all the other wavelengths. The CH_4 ice map produced by Schmitt et al. (2017) using the integrated band depth of the 1.7 μm band group has precisely these properties, and served as the basis for the registration.

We selected and processed a dataset of 12 approach images spanning about 5 days prior to the high-resolution images to create the global map (see Table 1 for detailed information). Three of the images within that chronological span (MET 298853429, 298940959 and 299064869) were skipped due to either their redundancy with another observation very close to it in time, or spectro-photometric calibration issues.

Given Pluto's rotation period of about 6.4 days, the sub-spacecraft longitude changed by about 288.5°, i.e. about 0.80 rotations. On the other hand, the sub-spacecraft latitude only changed by about 5.2°. Figure 2 shows that this dataset provides sufficient global coverage — evaluated using the initial misregistered data, but a comparison to the registered maps (Figures 4–7) show that the misregistration is low enough to not substantially change this.

The last, most high-resolution full-disk approach image (#12 in Table 1) was registered using the encounter-phase data as target image (HR1 & HR2 in Table 1, as well as UHR, which corresponds to the limited-coverage highest-resolution strip). This newly registered image was then used to register the previous image at slightly lower spatial resolution, and so on until the first selected approach phase image (e.g.#11 to #12, #10 to #11, etc. until #1 to #2). This was done in lieu of registering all the images directly to the high-resolution image, as the overlap between the highest- and lowest-resolution data used was too small to allow good registration.

#	Observation time (MET)	(UTC)	Resolution (km/px)	px/Pluto diameter	Sub-s/c lat (°N)	Sub-s/c long (°E)
1	298719334	2015-07-09 03:46:46	394.37	6.0	43.09	87.18
2	298767059	2015-07-09 17:02:14	353.51	6.7	43.07	56.06
3	298824624	2015-07-10 09:01:31	304.31	7.8	43.05	18.56
4	298854539	2015-07-10 17:22:47	278.59	8.5	43.03	358.96
5	298891829	2015-07-11 03:42:21	246.78	9.6	43.01	334.75
6	298939609	2015-07-11 16:58:32	205.88	11.5	42.99	303.66
7	298995539	2015-07-12 08:30:09	158.00	15	42.96	267.30
8	299026199	2015-07-12 17:01:49	131.85	18	42.92	247.35
9	299079314	2015-07-13 07:46:25	86.37	28	42.82	212.94
10	299105209	2015-07-13 13:59:33	64.10	37	42.70	196.19
11	299127869	2015-07-13 21:18:57	44.58	53	42.49	181.68
12	299144829	2015-07-14 02:01:50	30.23	79	42.15	171.14
HR1	299172014	2015-07-14 09:33:05	6.96	342	38.52	158.62
HR2	299172889	2015-07-14 09:48:16	6.20	383	37.91	158.81
UHR	299176809	2015-07-14 10:56:19	2.75	865	30.73	164.17

Table 1: List of Pluto approach-phase LEISA observations used, in chronological order, followed by the two high-resolution encounter-phase observations and the partial highest-resolution observation. The spatial resolution is given at the sub-spacecraft point.

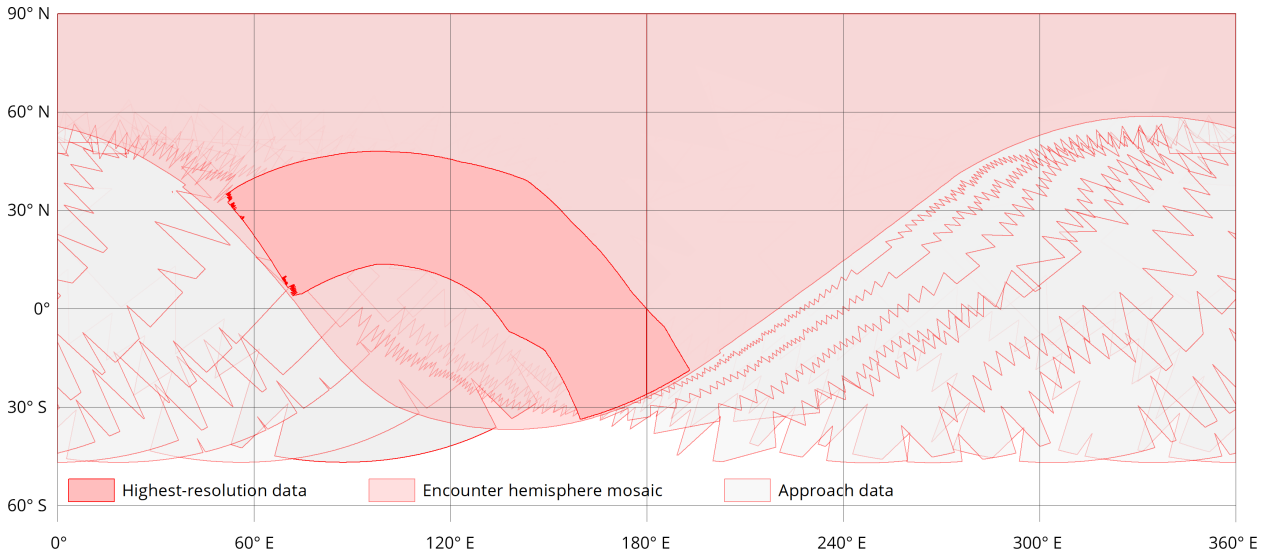

Figure 2: Global coverage obtained with the high-resolution (6-7 km/px) encounter dataset combined with the 12 approach images used (shown prior to registration). The highest-resolution (2.7 km/px) swath is also shown in dark red. The south pole is not shown as it is in polar night in the current season.

As mentioned before, once the transformation has been computed, it can be applied to any or all wavelengths in the hyperspectral image. For this paper we generated four main maps, corresponding to the spectral indices defined by Schmitt et al. (2017) as follows:

CH_4: integrated CH_4 band depth between 1.589 and 1.833 μm over a group of 3 CH_4 bands at 1.67, 1.72, and 1.79 μm.

$$BD(CH_4) = 1 - \frac{\int_{1.589\mu m}^{1.833\mu m} RF(\lambda)d\lambda}{\int_{1.589\mu m}^{1.833\mu m} Cont(\lambda)d\lambda} \tag{1}$$

N_2: integrated N_2 band depth between 2.121 and 2.160 μm over the N_2 band at 2.15 μm. The integration has been slightly extended to lower wavelengths compared to Schmitt et al. (2017), as we realised that the N_2 band wing contributes up to 2.12 μm in the wing of the strong 2.20 μm CH_4 band. This resulted in a slightly increased signal-to-noise ratio.

$$BD(N_2) = 1 - \frac{\int_{2.121\mu m}^{2.160\mu m} RF(\lambda)d\lambda}{1.5 * (RF_{2.105\mu m} + RF_{2.113\mu m} + RF_{2.1675\mu m} + RF_{2.1755\mu m})} \tag{2}$$

H_2O: spectral indicator using 10 wavelength bands centred around 1.39 and 2.06 μm.

$$SI(H_2O) = 1 - \frac{\int_{2.022\mu m}^{2.090\mu m} RF(\lambda)d\lambda}{\int_{1.365\mu m}^{1.410\mu m} RF(\lambda)d\lambda} \tag{3}$$

Red material: spectral indicator using the wavelength ranges around 1.430 and 1.658 μm.

$$SI(RedMat) = 1 - \frac{\int_{1.447\mu m}^{1.421\mu m} RF(\lambda)d\lambda}{\int_{1.670\mu m}^{1.641\mu m} RF(\lambda)d\lambda} \tag{4}$$

The BD(CH_4), SI(H_2O) and SI(RedMat) indices were calculated after processing the data cubes with a global PCA (over almost all spectral channels), followed by an inverse PC rotation on a selected number of axes to reduce noise and instrument artifacts. The BD(N_2) was calculated after similar processing, but over a restricted spectral range (40 wavelength bands) centred on the band peak (see Schmitt et al., 2017, for details). For the few lowest-resolution images, the PCA did not reduce the instrument artifacts because the number of pixels was insufficient for statistical evaluation, and so the PCA-processed data was not used.

2.3. Registration algorithm

We used intensity-based registration algorithms from SimpleITK (Lowekamp et al., 2013), a user-friendly Python interface to ITK. As we expect the misalignment between the datasets to be due entirely to imprecisions in the spacecraft pointing information, we restricted ourselves to global similarity transformations (i.e. translation, rotation, and scale). We used

an evolutionary algorithm-based optimiser and a Mattes mutual information metric (Mattes et al., 2001). The higher-resolution image was bilinearly resampled to the lower resolution, then both the source and target images were resampled to 2 km/px to allow for subpixel-level registration precision. A mask was applied to restrict the metric to the overlapping areas between both images. Table 2 shows the parameters used for the metric and optimiser.

Metric	Mattes mutual information
Number of bins	100
Percentage of pixels sampled	100%
Optimiser	1+1 evolutionary
Maximum iterations	20-100
Convergence tolerance	1.5×10^{-6}
Initial search radius	10^{-3}
Growth factor	1.01

Table 2: Registration parameters used.

3. Results

3.1. Validation of registration accuracy

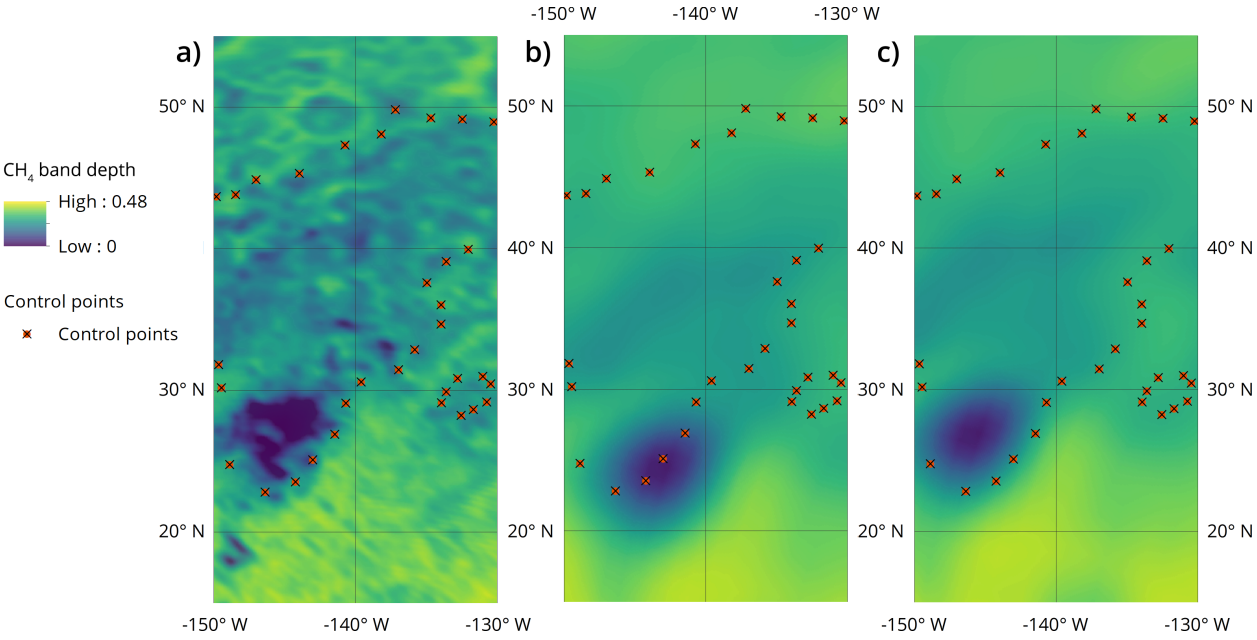

Figure 3: LEISA registration validation with control points: a) high-resolution data; b) misregistered low-resolution data (observation #10); c) registered low-resolution data.

The registration results were verified in two steps. First, those low-resolution images that had sufficient overlap with the high-resolution data were checked with a set of control points based on features identifiable in the high-resolution map. Figure 3 shows this for observation #11 as defined in Table 1. For observations #7–#12, registration was accurate within 0.5 native pixels.

Secondly, those observations which did not have enough overlap with the encounter hemisphere, or a sufficiently high resolution to do feature-based validation, were visually compared with the global panchromatic reflectance map produced by Schenk et al. (2018), as the 1.7 μm CH_4 band is very strongly correlated with the visible reflectance ($r = 0.655$ [2] as calculated using the high-resolution CH_4 map).

The second validation step showed that some latitudinal drift occurred for observations #1–#6. As their resolution was quite low (> 200 km/px), the maximum accuracy of any fit is limited by feature distortion. The transformation tended to overfit in trying to compensate, which was corrected by reducing the number of iterations for these six observations.

3.2. Composition maps

Figures 4 through 7 show the four registered global maps in simple cylindrical projection, at a sampling resolution of 2 km/px (which corresponds to a significant upsampling of the native resolutions of all approach-phase LEISA observations). Figure A.3 shows the same maps at the same resolution but in North polar orthographic projection. Figures 9 and 8 show the latitudinal and longitudinal distributions respectively for these four spectral indices, with binning resolutions of 2 px/° and 1 px/°. The latitudinal distributions have been weighted by the cosine of the latitude to recover the true surface area of the pixels and thus compensate the cylindrical projection. There is data at all longitudes down to 20°S latitude, and more limited longitude coverage down to about 40°S, close to the polar night limit at the time of the encounter. The detection limits and colormap ranges were taken from Schmitt et al. (2017).

Two additional maps were generated for further analysis, shown in Appendix A — the integrated band depth of the weak CH_4 band at 1.95 μm (Figure A.1, exact definition of band given in Schmitt et al., 2017), and a CH_4 band position index (Figure A.2), which is a metric representing the state of CH_4 at the surface, from CH_4 diluted in N_2-rich ice for the smaller index values to CH_4-rich ice for the highest. Intermediate values mean that both phases are present at the pixel scale, either spatially distributed, or intimately mixed at grain level, or stratified vertically.

The CH_4 integrated 1.7 μm band depth map (Figure 4) shows that the global longitudinal distribution of CH_4 (shown in Figure 8) is largely uniform across most of Pluto, albeit with

[2] Here and elsewhere in the paper r is the correlation coefficient weighted by the cosine of the latitude to account for the area distortion due to the cylindrical projection. The cutoffs for describing the correlation have been chosen as follows:

		$0.2 \leq \lvert r \rvert \leq 0.4$	correlated
$\lvert r \rvert < 0.05$	not correlated	$0.4 \leq \lvert r \rvert < 0.6$	strongly correlated
$0.05 \leq \lvert r \rvert < 0.20$	weakly correlated	$0.6 < \lvert r \rvert$	very strongly correlated

a clear depletion over the longitudinal range of Cthulhu Macula (70°E to 160°E, centered at (0°N, 90°E)). The latitudinal distribution of CH_4 (Figure 9) is more contrasted, with a global presence in the north polar areas, a more dispersed presence in the mid-northern latitudes and a strong CH_4 signal in a belt between 0 and 30°N from 160°E to 70°E. Both the CH_4-rich N polar cap and the equatorial CH_4 partial belt are clearly visible in the latitudinal distribution of the data in the isolated BT and SP subsets in Figure 9. The abundance of CH_4 seems also to increase below about 15°S, close to the shadowed south polar region. This last area is separated from the N tropical CH_4 belt by a S tropical belt of red material (see below).

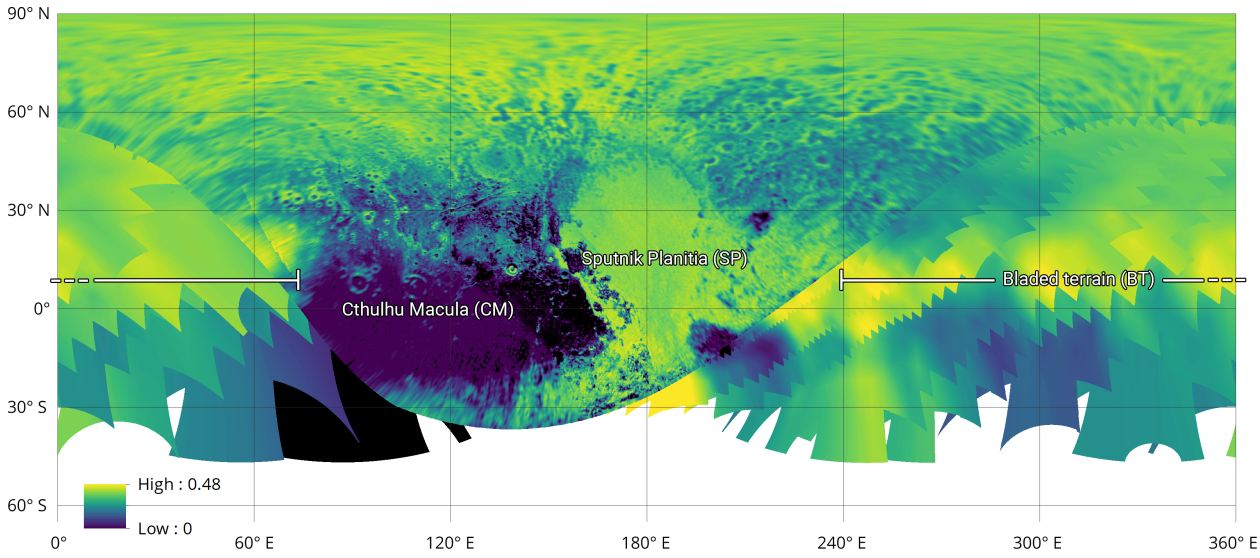

Figure 4: Global registered CH_4 1.7-μm integrated band depth map of Pluto, with the three largest geographical features labelled.

The N_2 band depth map (Figure 5) clearly shows the nitrogen-rich basin of Sputnik Planitia (centered at 20°N, 179°E), easily identifiable as a bump in the centre of the longitudinal distribution (Figure 8). We also see an asymmetry around 180°E which reflects the east-west contrast in ice composition within SP (the bright and dark plains). N_2 ice is also strongly present in a northern belt between 30°N and 75°N, with a strong peak around 43°N (Figure 9), as well as in the N tropical CH_4 belt (E of 180°) with a peak around 20°N in phase with the one of CH_4. Its correlation with the 1.7 μm CH_4 band is not very strong, but positive ($r = 0.189$). Due to the weakness of the N_2 band and the low signal-to-noise close to the terminator it is difficult to confirm that an increase of N_2 seen SW of Sputnik Planitia in the high-resolution part of the map also occurs below about 15–20°S at all longitudes, and that may be correlated with the mid-southern latitude increase of CH_4 ice seen at least between 100°E and 280°E (Figure 4).

The H_2O spectral index map (Figure 6) shows water ice presence between 50°N and 30°S. This overlaps with the global red material belt as seen on Figure 7, which fills the space between 10°N and 20°S except at Sputnik Planitia — although small quantities of

red material are indeed visible in the dark plains of SP. There are only small differences between the red material and H_2O distributions, as they seem well-correlated when the red material is moderately abundant but start to be anti-correlated when it is very abundant, as in the centre E of Cthulhu Macula (115–160°E), E of Krun Macula (220°E) and Balrog Macula (280°E). This correlation was already evident from the high-resolution map, but is now confirmed globally ($r = 0.490$).

A small bump of red material abundance also occurs just above 30°N (Figure 9). The overabundance of H_2O both between 70–160°E and 195–220°E is due to a combination of the presence of large maculae (Cthulhu, Krun) at S tropical latitudes and concentrated water ice spots at mid-northern latitudes (30°N) at these longitudes. As expected, both the H_2O ice and the red material are quite strongly anti-correlated with the 1.7 μm CH_4 band ($r = -0.751$ and $r = -0.757$ respectively).

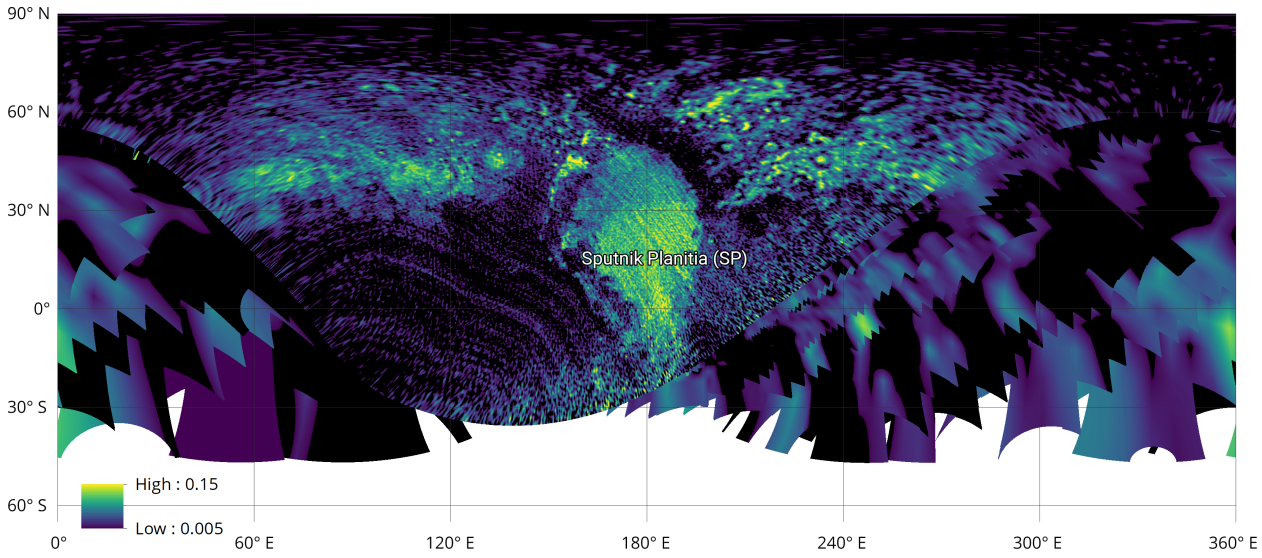

Figure 5: Global registered N_2 2.15-μm band depth map of Pluto, with Sputnik Planitia labelled. The detection limit is at a value of 0.005.

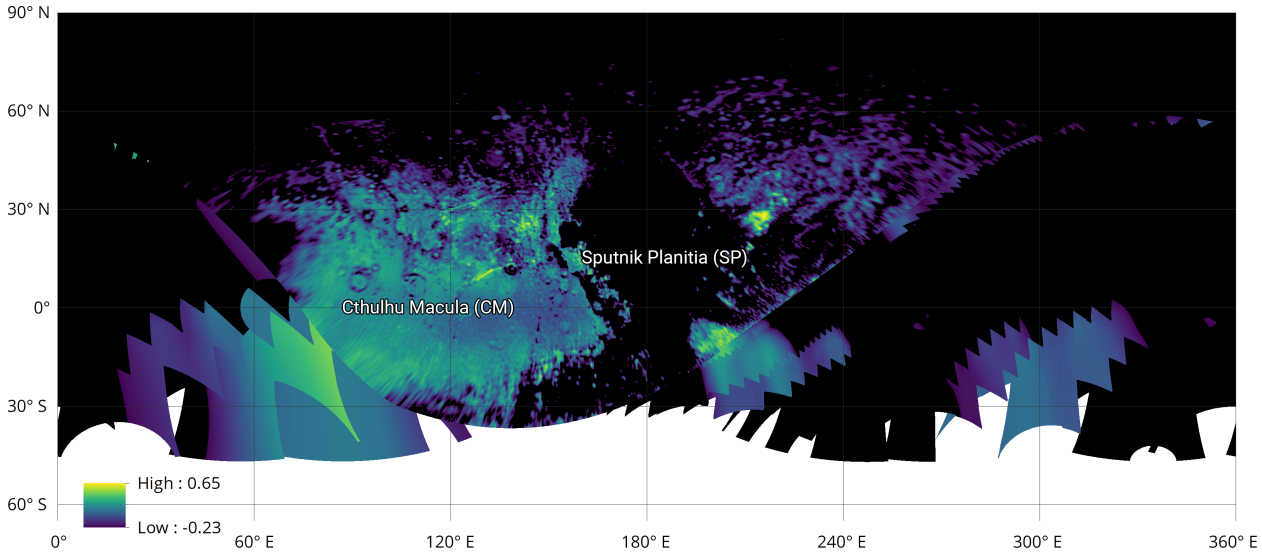

Figure 6: Global registered H_2O spectral index map of Pluto, with Cthulhu Macula and Sputnik Planitia labelled. The detection limit is at an index value of -0.23.

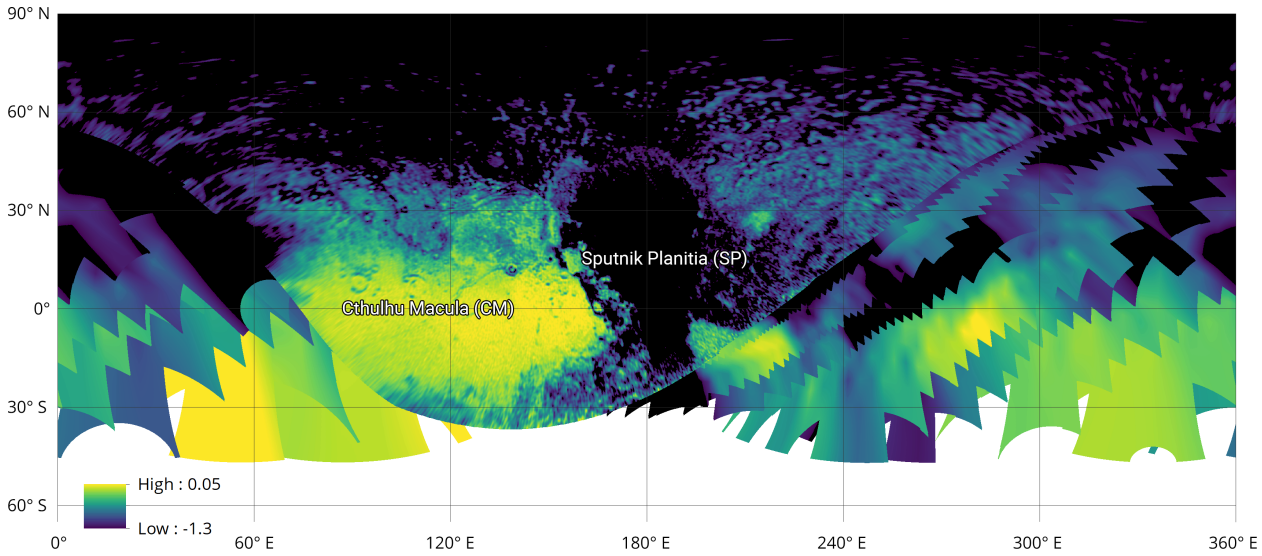

Figure 7: Global registered red material spectral index map of Pluto, with Cthulhu Macula and Sputnik Planitia labelled. The detection limit is at an index value of -1.3.

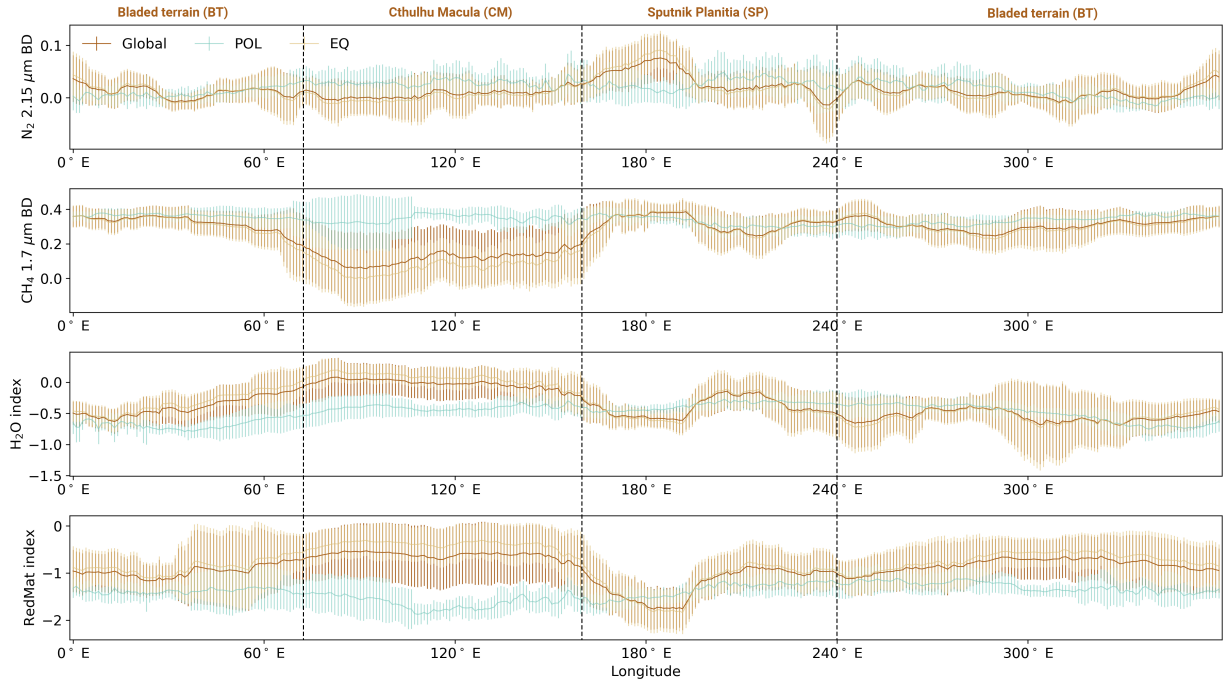

Figure 8: Distribution of LEISA dataset band depth and index values as a function of longitude, binned at 1 pixel per degree. The distribution is computed for the global dataset, for the mid-to-equatorial latitudes (0–45°, labelled EQ), and for the mid-to-polar latitudes (45–90°, labelled POL). The points represent the mean value over latitude for that longitude range and the error bars are the standard deviation. The distributions are weighted by cos(lat) to compensate for the cylindrical projection.

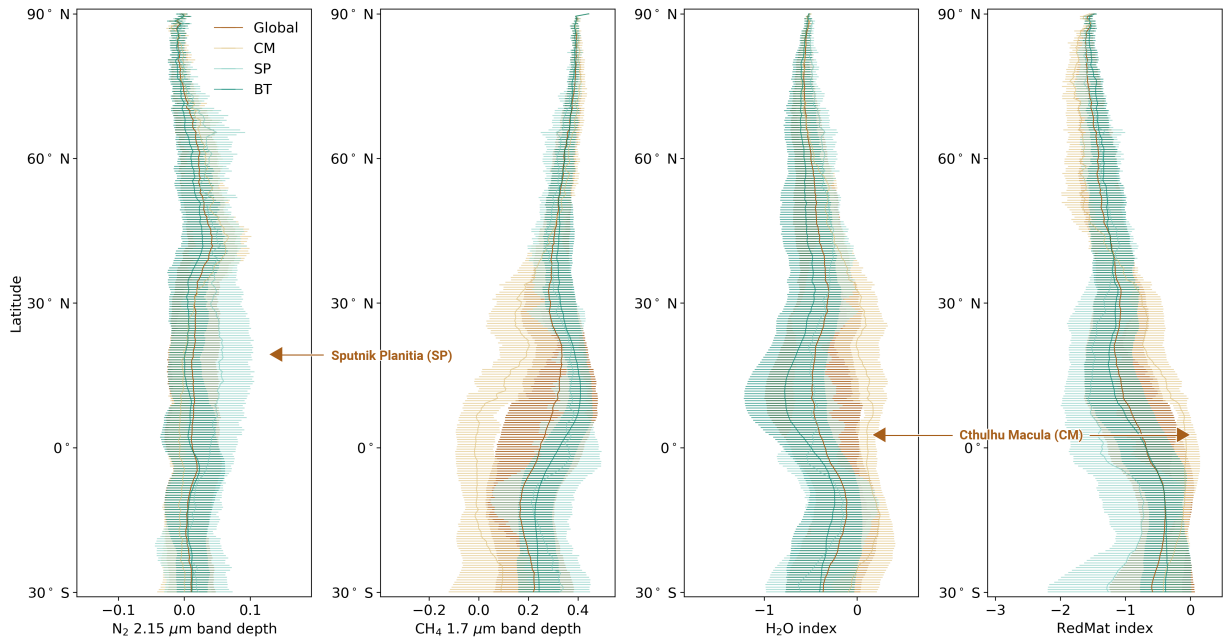

Figure 9: Distribution of LEISA dataset band depth and index values as a function of latitude, binned at 2 pixels per degree. The distribution is computed for the global dataset, for the Cthulhu Macula latitude range (70–160°E, labelled CM), for the Sputnik Planitia latitude range (160–240°E, labelled SP), and for the bladed terrain range (0–70 and 240–360°E, labelled BT). The points represent the mean value over longitude for that latitude range and the error bars are the standard deviation.

4. Discussion

4.1. Analysis of correlations between the LEISA maps

In addition to computing the simple correlation coefficients between the different LEISA maps, we also computed the full 2D correlations in order to identify spatially localised populations. The more significant of these correlations are shown as hexagonal bin plots in Figure 10, and may be compared with some of the same calculations carried out for the high-resolution hemisphere by Schmitt et al. (2017).

Figure 10a shows multiple trends within the global positive correlation between the 2.15-μm N_2 and 1.7-μm CH_4 integrated band depths:

- a vertical trend, with variable CH_4 band depth and negative N_2 band depth (marked in red) that corresponds to fine- to coarse-grained CH_4-rich ice.
- a negative correlation trend, going from strong CH_4 values and absent N_2 to strong N_2 and weak CH_4 values (marked in orange), corresponding to coarse-grained N_2-rich ice containing low to medium amounts of dissolved CH_4 ($<$1%).

- a horizontal trend with high CH_4 band depth and variable N_2 values (marked in yellow), that corresponds to very coarse-grained CH_4-rich ice (>20 cm) with a high CH_4 content (>1%).

These trends correspond largely to those seen in Figure 18A of Schmitt et al. (2017), and we used the terrain classes identified by the latter as well as a Gaussian mixture clustering model(Li et al., 2013) as implemented in scikit-learn (Pedregosa et al., 2011) to generate a classification of the global map, shown in Figure 12.

Figure 10b shows the correlation between the N_2 integrated band depth map and the CH_4 band position index map (i.e. the CH_4 state map). We observe a global anti-correlation (marked in orange) that can be classified into a spectrum of terrains going from N_2-rich to CH_4-rich, as shown by Schmitt et al. (2017) in their figures 22 and 39 for the encounter hemisphere. We compute a similar classification for the global map and show it in Figure 13.

Figure 10c shows a simple strong linear correlation between the H_2O and red material spectral indices. A global segmentation of the four types of terrains shown visible in this correlation plot is presented in Figure 11. The pixels which have a positive value for both datasets correspond to the top right (yellow) quadrant. There is, however, a number of pixels in Figure 10c displaying an anti-correlation, i.e. a positive presence of red material but without detection of H_2O ice (top left quadrangle, blue). They correspond mostly to the centre of the maculae, where the red material either fully covers the water ice crust or is mixed with sufficient quantities of N_2 and CH_4 ice to attenuate the water ice signal. On the other hand, there are clearly only very few pixels with pure water ice without red material (bottom right quadrangle, green). The bottom left quadrangle (purple) corresponds to the terrains fully covered by N_2-rich and/or CH_4-rich volatile ices, thus hiding the non-volatile materials. We can clearly see this anti-correlation between volatile ices and red material in Figure 10d, trend line marked in orange.

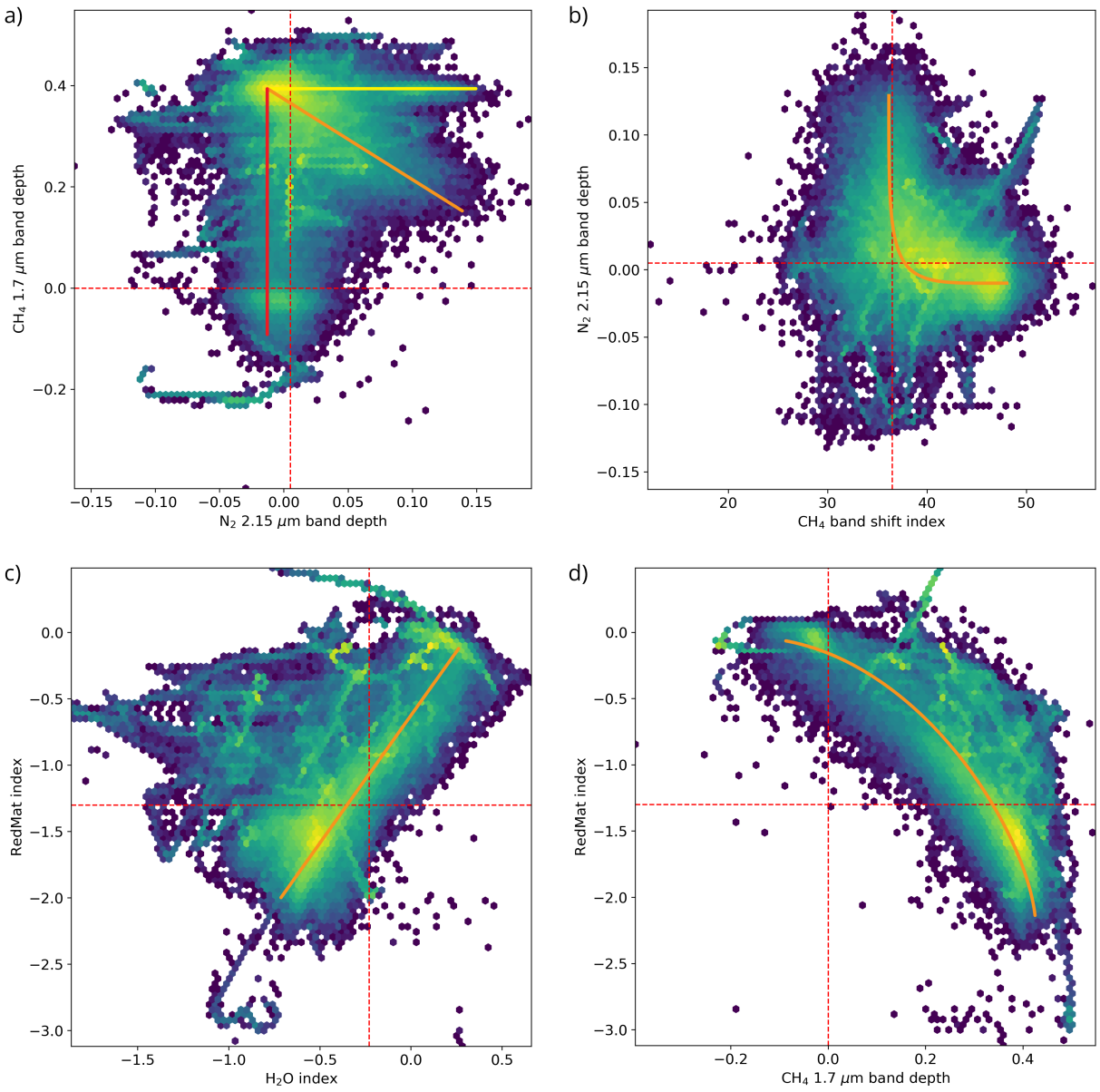

Figure 10: Hexagonal bin plots showing correlations between different LEISA maps. The detection thresholds for each map are marked with a red dotted line, and correlation trends are marked with solid lines.

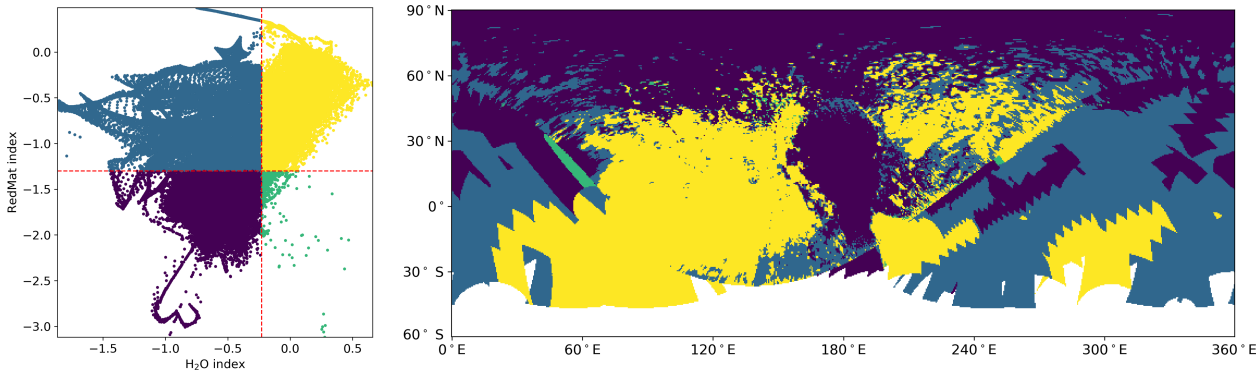

Figure 11: Global classified map based on the correlation plot of the H_2O and RedMat spectral indices, defined by the dataset detection thresholds.

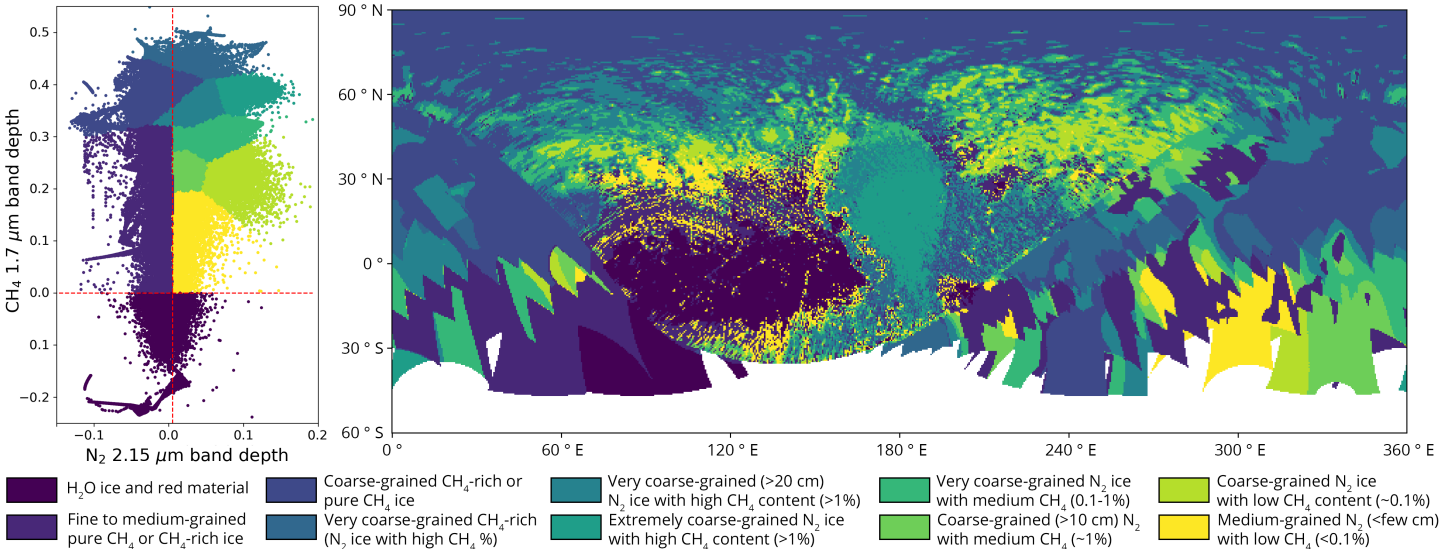

Figure 12: Global classified map based on the correlation plot of the N_2 and 1.7 μm CH_4 integrated band depths, calculated with a Gaussian mixture clustering model.

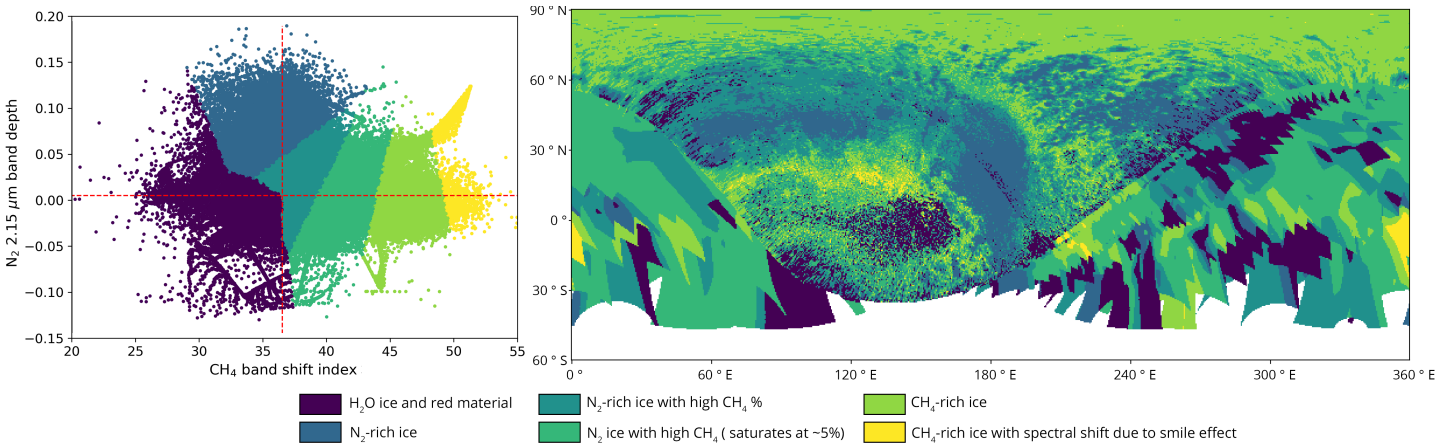

Figure 13: Global classified map based on the correlation plot of the CH_4 band position index (CH_4 state index) and N_2 integrated band depth, calculated with a Gaussian mixture model.

4.2. Comparison with MVIC maps

Figures 14 and 15 show the methane narrow-band (980 nm) equivalent width map and the global spectral slope map obtained by Earle et al. (2018) from the analysis of the MVIC dataset and plotted with a similar colour scale to our maps derived from the LEISA dataset. Figure 16 shows the 2D correlations between these two maps and several of the LEISA maps.

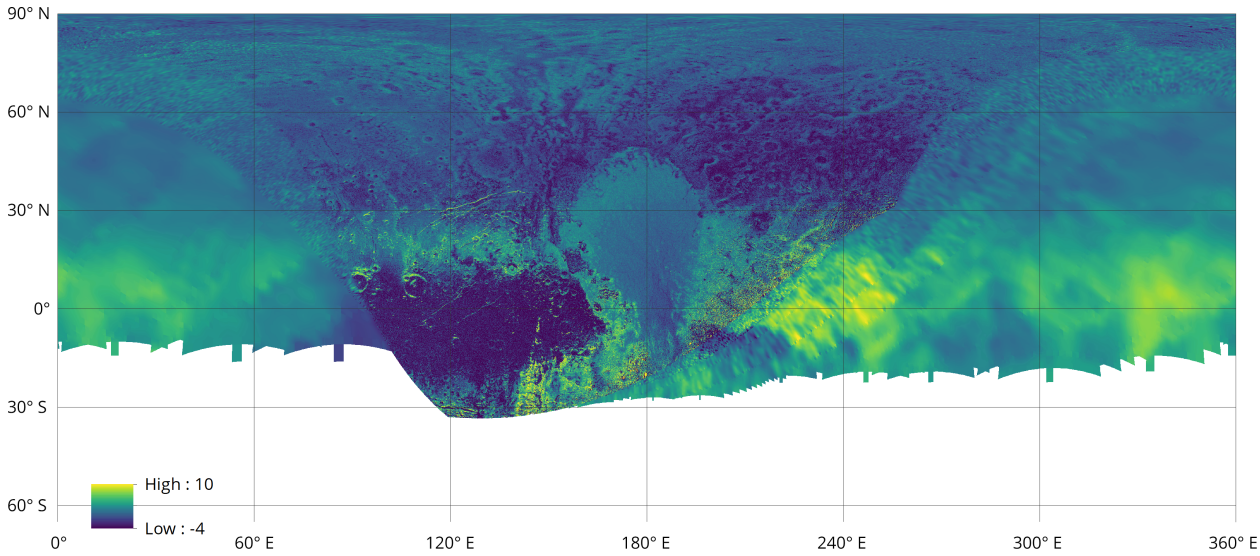

Figure 14: Global mosaic of the MVIC equivalent width of the 980 nm methane absorption band, produced by Earle et al. (2018).

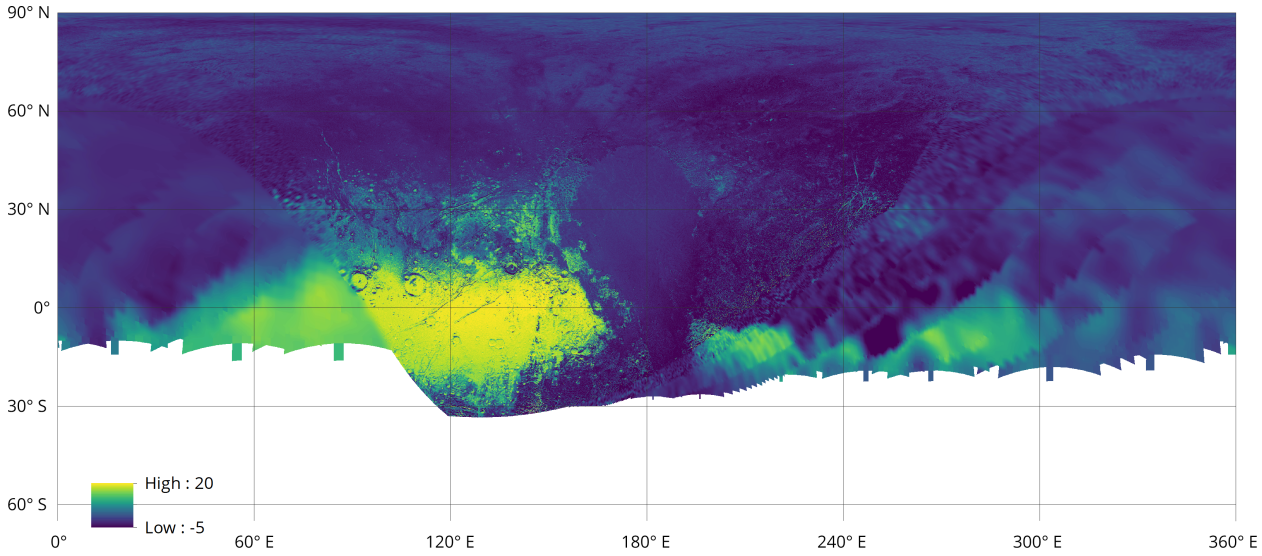

Figure 15: Global mosaic of the MVIC spectral slope map in reflectance %/100 nm, produced by Earle et al. (2018).

The LEISA strong-band 1.7 μm CH_4 band depth map is somewhat correlated with the MVIC 980 nm-band CH_4 map ($r = 0.445$), but Figure 16a shows that there is no single strong trend to be identified in the correlation plot. We expected the weak-band 1.95 μm CH_4 band depth map to be more strongly correlated with the MVIC 980 nm band, and while the overall correlation is slightly stronger ($r = 0.531$), the correlation plot (Figure 16b) again shows no particularly strong trends. In particular, both LEISA band depth maps display areas with abundant methane where MVIC did not see any, or at very weak levels (bottom right quadrangles and in particular the yellow spot along the right part of the red horizontal line in both figures). Conversely, over a number of pixels MVIC has positive detection of CH_4 where LEISA detects none of the CH_4 bands (upper left quadrangle). Figure 17 shows which spatial regions these quadrangles correspond to. We can see that the LEISA-only values (in green) are present almost exclusively in the high-resolution data, while conversely the MVIC-only values (in blue) are seen largely in the low-resolution part of the map. This seems to suggest that while the encounter-phase LEISA measurements are more sensitive to CH_4 than MVIC, the signal averaging that occurs at lower resolutions means this sensitivity is lost.

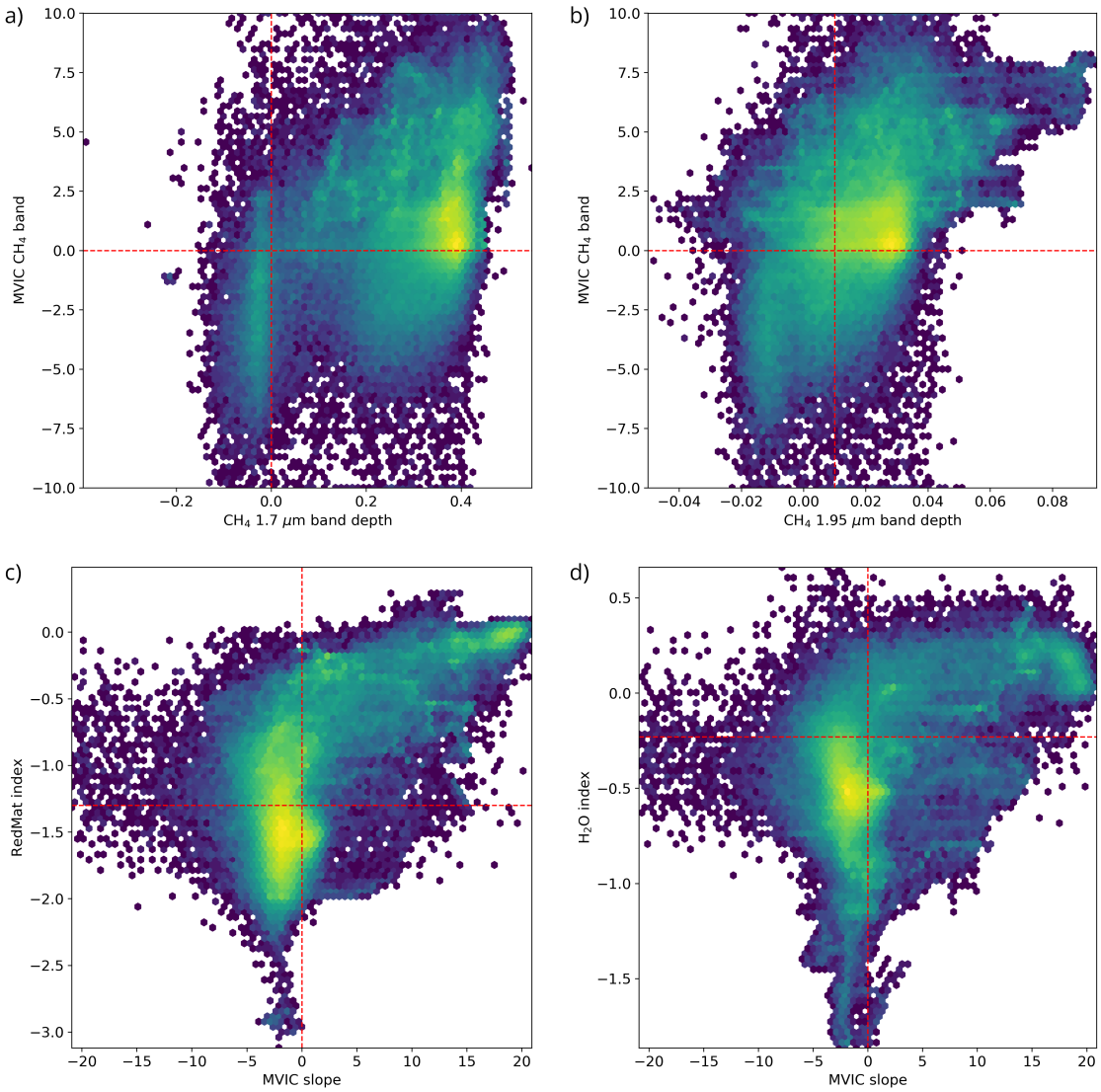

Figure 16: Hexagonal bin plots showing correlations between different LEISA maps and the MVIC maps. The detection thresholds for each map are marked with a red dotted line.

In Figure 16c and d we see that the MVIC slope map is correlated relatively strongly with the red material spectral index ($r = 0.675$) as well as the H_2O spectral index ($r = 0.529$), with overall similar distributions. The latter figure is consistent with the correlation and terrain classification calculated by Schmitt et al. (2017) for the H_2O spectral index, and we adapt their terrain definitions to produce a similar classification (Figure 18).

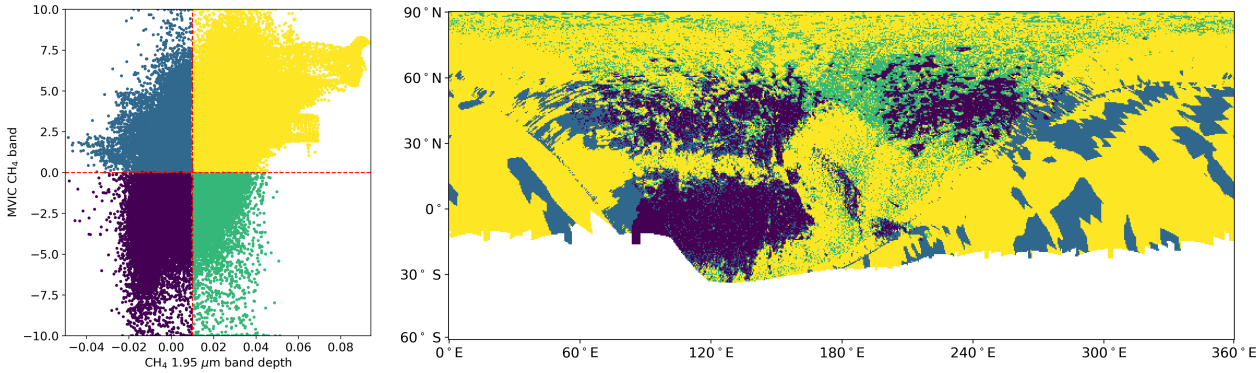

Figure 17: Global classified map based on the correlation plot of the LEISA CH_4 1.95 μm band depth map and the MVIC CH_4 980 nm band map, defined by the dataset detection thresholds.

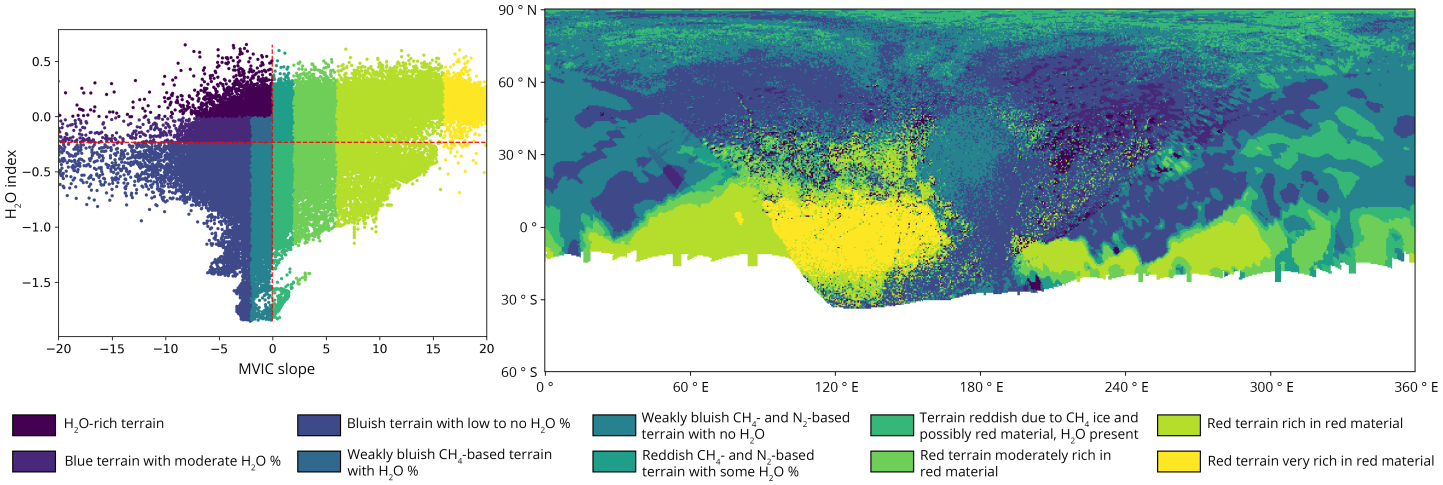

Figure 18: Global classified map based on the correlation plot of the H_2O spectral index and MVIC slope, defined from a Gaussian mixture model and the segmentation in (Schmitt et al., 2017).

Earle et al. (2018) also developed a terrain classification based on the MVIC CH_4 and slope maps (see their Fig. 15). The six terrain types established are: **pure CH_4-rich**; **CH_4-rich diluted with N_2**; **N_2- or CO-rich areas with some CH_4**; **mix of CH_4 and tholins**; **moderate tholin deposits with some CH_4**; and **substantial tholin deposits with little/no CH_4**. Figure 19 shows histograms for the four LEISA band depths (N_2, 1.7 μm CH_4) and spectral indices (H_2O and red material) within these six terrain types.

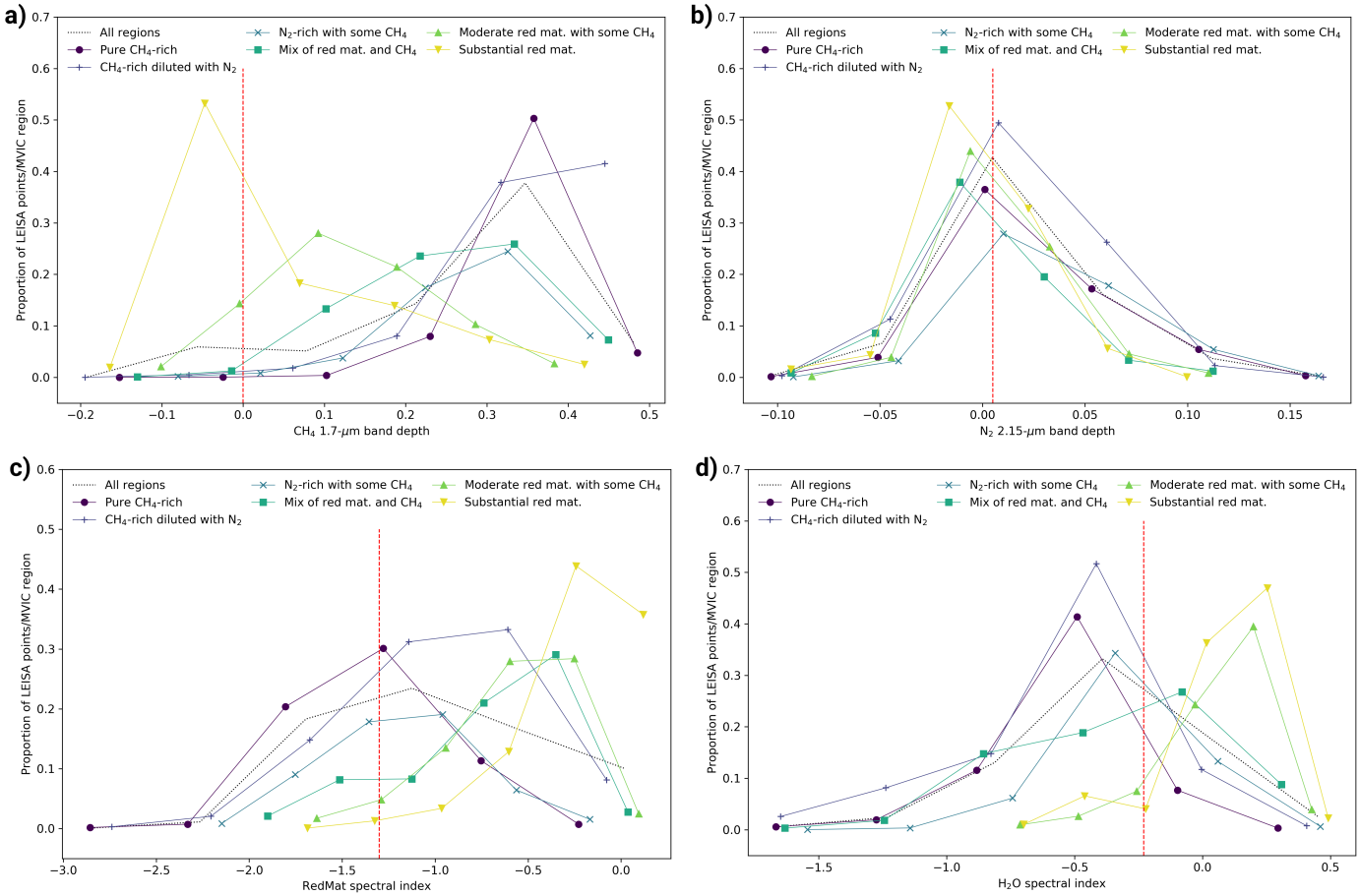

Figure 19: Histograms of the value distribution of the four LEISA maps (N_2 and 1.7 μm CH_4 band depths, H_2O and red material spectral index) for the six MVIC terrain types, weighted to compensate for distortion due to the cylindrical projection and normalised to the terrain area.

The global methane-rich belt between 0 and 30°N largely corresponds to the "pure CH_4-rich" terrain type on the MVIC terrain map (band depth mean $\mu = 0.359$, $\sigma = 0.056$), and the diluted methane presence at mid-northern latitudes relatively well corresponds to the "CH_4-rich diluted with N_2" terrain ($\mu = 0.352$, $\sigma = 0.091$), as shown in Figure 19a. The histograms extracted from the N_2 band depth map (Figure 19b) show N_2 presence within both the "N_2-rich with some CH_4" and "CH_4-rich with N_2" MVIC terrain types, but also in all other MVIC terrain types. As expected, the MVIC channels are only poorly sensitive to the presence of N_2 ice through the general anti-correlation between the presence of volatile ices and the red slope produced by the red material, due to the segregation of both components through sublimation-condensation cycles. Even if the LEISA N_2 band depth is not a direct measurement of the abundance of nitrogen ice at the surface, and is sensitive to other parameters such as grain size and CH_4 abundance, it is far more sensitive to its presence than the MVIC data. Looking at the N_2 and CH_4 band depth-based classification in Figure 12, we can see several distinct regions corresponding to various coarse-grained N_2-

rich ices with high to medium CH_4 content that are not mapped as containing N_2 ice using the MVIC CH_4-band/red slope classification alone.

The LEISA red material spectral index map (Figure 7, histograms in Figure 19c) corresponds primarily to the "substantial tholin deposits" terrain type (spectral index mean $\mu = -0.205, \sigma = 0.274$), while the spectral index for the two tholin-CH_4 mixed terrain types is significantly lower ("moderate tholin deposits, some CH_4": $\mu = -0.576$, $\sigma = 0.348$; "mix of CH_4 and tholins": $\mu = -0.706$, $\sigma = 0.463$). Our red material indices are thus well-correlated in the terrains dominated by this material. The H_2O ice spectral index map exhibits a similar distribution to the red material map (Figure 19d), with the strongest presence in the "substantial tholin deposits" terrain ($\mu = 0.090$, $\sigma = 0.212$) and in the "moderate tholin deposits, some CH_4" terrain ($\mu = 0.064$, $\sigma = 0.208$). This is consistent with the LEISA-based classification in Figure 18 and confirms that H_2O ice is mostly spatially coincident with the red material.

4.3. Composition relationship with geology

We are able to evaluate the relationship between the LEISA composition maps and the geology of Pluto's surface using the LORRI panchromatic reflectance map and the digital elevation model (Figure 20) produced by Schenk et al. (2018).

While both the LEISA CH_4 and N_2 maps (Figures 4 and 5) are globally anti-correlated with altitude, this is largely due to the massive presence of the convective Sputnik Planitia basin, which is N_2-rich with some diluted CH_4. The two maps are strongly anti-correlated with altitude for the area of the DEM containing Sputnik Planitia (between 140 and 200°E and south of 40°N, $r(CH_4) = -0.501$ and $r(N_2) = -0.569$), but outside this area CH_4 is positively correlated with the DEM ($r = 0.211$), while the N_2 anti-correlation is much weaker than it is within SP ($r = -0.161$). The two separate populations of CH_4 and N_2 terrains can also be clearly seen in the 2D hexagonal bin correlation plots (see Appendix B).

These CH_4-rich elevations appear to mostly correspond to the bladed terrains as described in Moore et al. (2018), and can be visually identified in the LEISA 1.7 μm CH_4 map as the methane-rich belt between 0 and 30°N. The N_2-rich medium-altitude areas, accordingly, correspond to the smooth plains present in the bright pitted uplands as described in Moore et al. (2016), and are identifiable between 30°N and the equator as well as intermittently between 0 and 30°S. Figure 21 and 22 show an overlays of the CH_4 and N_2 maps respectively over the DEM, where these terrains can be seen.

The CH_4 and N_2 presence in this belt extends fully across the low-resolution hemisphere, and so we may posit that the "bright pitted upland and bladed terrain"-type landscape also continues eastward across Pluto until approximately 80°E, although it is mostly coated with dark red material in the southern part of the belt between 0 and 30°S.

Calculating the correlations between the datasets as a function of latitude (see Appendix C) shows that in addition to the equatorial methane belt, the CH_4 1.7 μm band depth is also correlated with altitude at higher latitudes (between 40 and 80°N, peaking at 60°N). These CH_4-rich uplands match the dissected and eroded terrains described in Moore et al. (2016), while the lower-altitude N_2-rich areas within them correspond to the smooth infill of the pits and depressions contained in these terrains.

Conversely, while H_2O ice is globally slightly correlated with altitude ($r = 0.118$), the latitude- and longitude-dependent correlation plots show that elevated water-ice terrains are found primarily in two latitudinal belts, at about 30°N and 10°S, and that within the encounter hemisphere they are restricted to the 150-180°E range. This suggests that the global H_2O–altitude correlation is due mostly to the water-ice mountain ranges bordering the west side of Sputnik Planitia (Howard et al., 2017; White et al., 2017), and water ice found elsewhere corresponds mostly to partially exposed substrate terrain, underlying either a layer of red material at sub-equatorial southern latitudes or CH_4-rich uplands at northern latitudes. This is supported by computing the H_2O–DEM correlation for the SP area (strongly positive, $r = 0.448$) separately from the rest of the DEM (negative, $r = -0.221$).

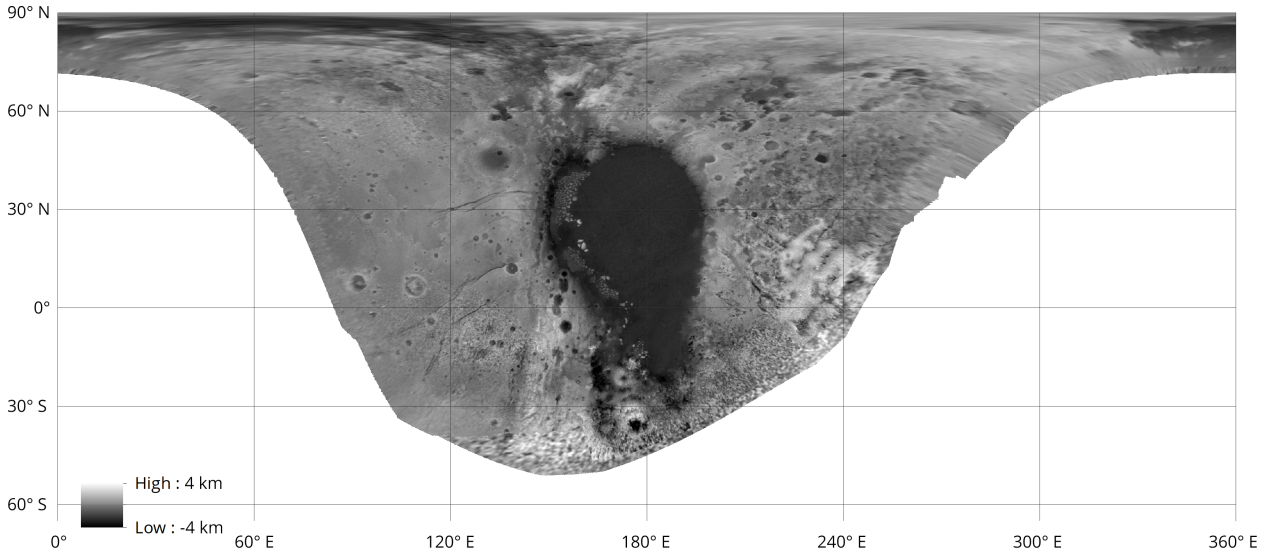

Figure 20: Global digital elevation model of Pluto produced using stereogrammetric analysis of LORRI and MVIC stereo scans (Schenk et al., 2018).

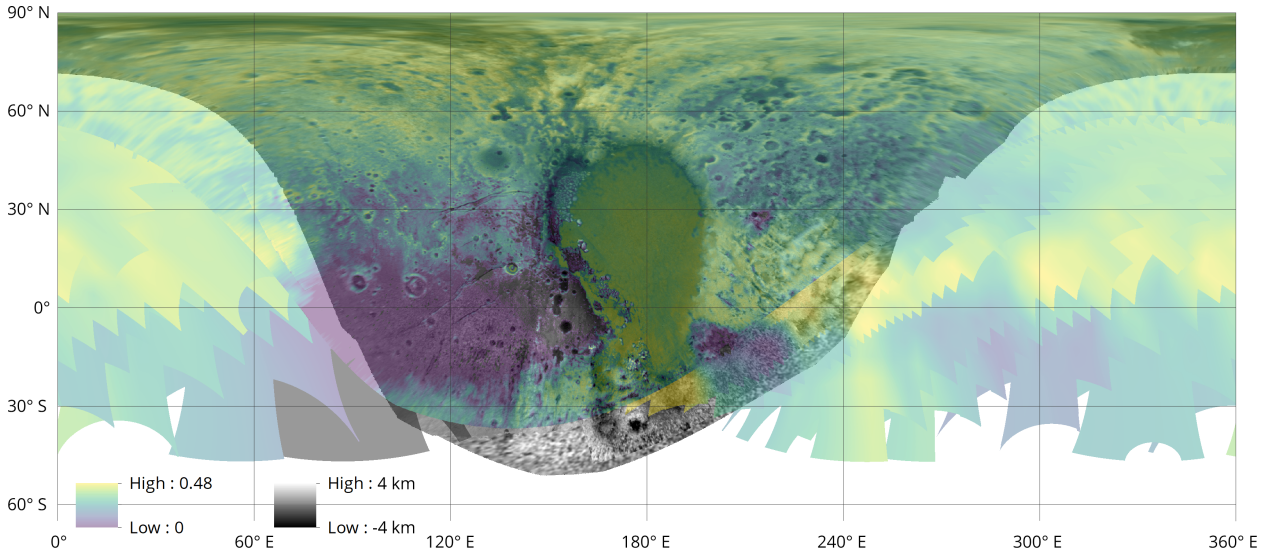

Figure 21: Global LEISA CH_4 1.7 μm band depth map overlaid over the digital elevation model of Pluto.

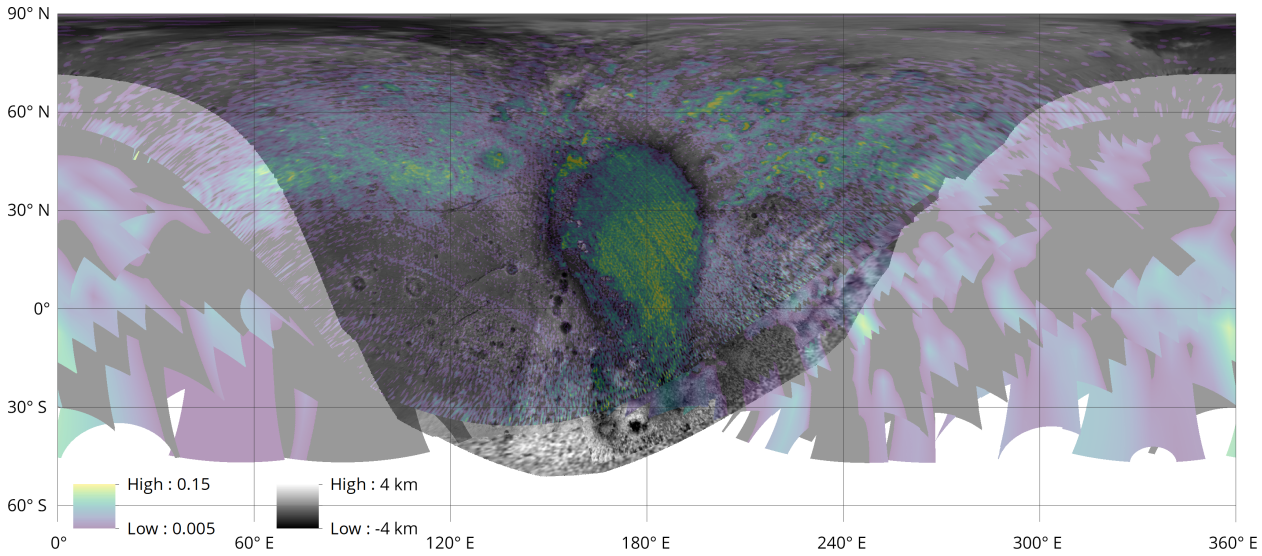

Figure 22: Global LEISA N_2 2.15 μm band depth map overlaid over the digital elevation model of Pluto.

4.4. Utility of global composition maps for atmospheric circulation

Bertrand et al. have dedicated multiple works (Bertrand and Forget, 2016; Bertrand et al., 2018, 2019) to simulating the long-term volatile transport history that would result in a present-day ice reservoir distribution coherent with New Horizons observations. These studies have relied on composition information from both the high-resolution hemisphere LEISA data and the global MVIC maps, but have not been able to take into account global

composition maps from hyperspectral data, which will provide more accurate information on both the latitudinal and longitudinal asymmetries of the volatile ice reservoirs as well as on their total volume. Notably, Bertrand et al. (2018) mention that the location of perennial N_2 ice deposits should depend on the brightness of mid-to-polar CH_4 deposits, which can be more easily quantified with a global map. Additionally, Bertrand et al. (2019) predicts the deposition pattern of N_2 outsite of Sputnik Planitia to consist of very localized patchy deposits in the equatorial deep depressions of the BT and mid-latitude deposits ($\pm$30–60°). This was consistent with the encounter hemisphere maps already released by Schmitt et al. (2017) and Protopapa et al. (2017) but can now be verified globally and can be easily observed to be true from the latitudinal map distributions (Figure 9). All types of global or local energy balance models or climatic models will benefit from these new global maps of the different materials present at the surface of Pluto, either as an input to calculate the current thermal balance of the planet, or as a constraint for the current volatile ice distribution to be obtained (e.g. Lewis et al., this special issue, submitted; Johnson et al., this special issue, submitted; Bertrand et al., submitted).For a more specific example, as on Pluto the general atmospheric circulation is driven by the N_2 condensation–sublimation flows, the global maps of distribution of surface N_2 ice are key to allow simulating realistic atmospheric circulation.

5. Conclusion

5.1. Global compositional cartography

We have co-registered a dataset of low-resolution LEISA hyperspectral images, recorded during the approach phase, with the high-resolution closest-approach data from the New Horizons encounter with Pluto, and produced global maps for the following spectral indicators:

1. CH_4 1.7 μm integrated band depth
2. N_2 2.15 μm integrated band depth
3. H_2O spectral index
4. Red material spectral index

We compare these maps with other global Pluto datasets based on LORRI (topography and panchromatic reflectance (Schenk et al., 2018)) and MVIC measurements (980 nm CH_4 band and spectral slope) (Earle et al., 2018), as well as previous works on the high-resolution LEISA dataset (Schmitt et al., 2017; Protopapa et al., 2017). We are able to globally confirm the latitudinal composition variation proposed by Protopapa et al. (2017) — a red carbonaceous material belt between 0 and 30°S, an accumulation of CH_4-rich ice between 0 and 30°N in the anti-encounter hemisphere (opposing SP and CM), a mixture of N_2-rich terrains with some CH_4-rich areas between 30 and 60°N, and a CH_4-rich North polar area — which also corresponds well to the categorisation of CH_4 and red material terrains based on MVIC data presented in Earle et al. (2018). In addition, the LEISA data allowed us to correctly map globally the presence of both N_2 and H_2O ices.

Based on the composition maps' correlation with geology and topography we also propose geological interpretations for compositional features in the anti-encounter hemisphere, such as:

- the presence of CH_4-rich dissected/eroded terrain in high latitudes, especially enriched in CH_4 at high altitude,
- further evidence of an interrupted/partial equatorial belt of CH_4-rich bladed terrain punctuated with N_2-rich lowlands,
- and exposed H_2O ice substrate at longitudes outside Sputnik Planitia.

5.2. Evaluation of intensity-based registration

This study is one of the first applications of intensity-based registration in planetary cartography, and shows the promising potential of this tool. Figure 3 shows the sub-pixel accuracy of the technique in the regions that can be verified using control points based on the high-resolution data, and this validation method shows that the accuracy remains constant when co-registering maps with resolutions as low as 158 km/px (the lowest tested resolution) and no easily-delineable features. While intensity-based registration alone becomes insufficient when working with significantly lower resolutions, it can be easily combined with a large-scale feature-based algorithm that helps maintain common-sense constraints (e.g. making sure the object being mapped remains within its possible range of boundaries) to create a fully automated all-purpose registration algorithm.

Acknowledgements

This work was supported by the CNES. It is based on observations with RALPH/LEISA embarked on New Horizons.

References

References

Bertrand, T., Forget, F., 2016. Observed glacier and volatile distribution on Pluto from atmosphere–topography processes. Nature 540, 86–89. doi:10.1038/nature19337.

Bertrand, T., Forget, F., Umurhan, O., Grundy, W., Schmitt, B., Protopapa, S., Zangari, A., White, O., Schenk, P., Singer, K., Stern, A., Weaver, H., Young, L., Ennico, K., Olkin, C., 2018. The nitrogen cycles on Pluto over seasonal and astronomical timescales. Icarus 309, 277–296. doi:10.1016/j.icarus.2018.03.012.

Bertrand, T., Forget, F., Umurhan, O., Moore, J., Young, L., Protopapa, S., Grundy, W., Schmitt, B., Dhingra, R., Binzel, R., Earle, A., Cruikshank, D., Stern, S., Weaver, H., Ennico, K., Olkin, C., 2019. The CH_4 cycles on Pluto over seasonal and astronomical timescales. Icarus 329, 148–165. doi:10.1016/j.icarus.2019.02.007.

Bertrand, T., Forget, F., White, O., Schmitt, B., submitted. Pluto's beating heart regulates the atmospheric circulation: results from high resolution and multi-year numerical climate simulations. J. Geophys. Res. E .

Buie, M.W., Grundy, W.M., Young, E.F., Young, L.A., Stern, S.A., 2010. Pluto and Charon with the Hubble Space Telescope. II. Resolving changes on Pluto's surface and a map for Charon. The Astronomical Journal 139, 1128–1143. doi:10.1088/0004-6256/139/3/1128.

Earle, A.M., Grundy, W., Howett, C.J.A., Olkin, C.B., Parker, A.H., Scipioni, F., Binzel, R.P., Beyer, R.A., Cook, J.C., Cruikshank, D.P., et al., 2018. Methane distribution on Pluto as mapped by the New Horizons Ralph/MVIC instrument. Icarus 314, 195–209.

Grundy, W., Buie, M., 2001. Distribution and evolution of CH4, n2, and CO ices on pluto's surface: 1995 to 1998. Icarus 153, 248–263. doi:10.1006/icar.2001.6684.

Grundy, W., Olkin, C., Young, L., Buie, M., Young, E., 2013. Near-infrared spectral monitoring of pluto's ices: Spatial distribution and secular evolution. Icarus 223, 710–721. doi:10.1016/j.icarus.2013.01.019.

Howard, A.D., Moore, J.M., Umurhan, O.M., White, O.L., Anderson, R.S., McKinnon, W.B., Spencer, J.R., Schenk, P.M., Beyer, R.A., Stern, S.A., Ennico, K., Olkin, C.B., Weaver, H.A., Young, L.A., 2017. Present and past glaciation on Pluto. Icarus 287, 287–300. doi:10.1016/j.icarus.2016.07.006.

Johnson, P.E., Young, L.A., Protopapa, S., Schmitt, B., Gabasova, L.R., Lewis, B.L., Stansberry, J.A., Mandt, K.E., White, O.L., this special issue, submitted. Modeling Pluto's minimum pressure: implications for haze production. Icarus .

Lewis, B.L., Stansberry, J.A., Holler, B.J., Grundy, W.M., Schmitt, B., Protopapa, S., Stern, S.A., Young, L., Weaver, H.A., Olkin, C., Ennico, K., the New Horizons Science Team, this special issue, submitted. Distribution and energy balance of PlutoâĂŹs nitrogen ice, as seen by New Horizons in 2015. Icarus .

Li, W., Prasad, S., Fowler, J.E., 2013. Hyperspectral image classification using Gaussian mixture models and Markov random fields. IEEE Geoscience and Remote Sensing Letters 11, 153–157.

Liang, J., Liu, X., Huang, K., Li, X., Wang, D., Wang, X., 2014. Automatic registration of multisensor images using an integrated spatial and mutual information (SMI) metric. IEEE transactions on geoscience and remote sensing 52, 603–615.

Lowekamp, B.C., Chen, D.T., Ibáñez, L., Blezek, D., 2013. The design of SimpleITK. Frontiers in neuroinformatics 7, 45.

Mattes, D., Haynor, D.R., Vesselle, H., Lewellyn, T.K., Eubank, W., 2001. Nonrigid multimodality image registration, in: Medical imaging 2001: image processing, SPIE. pp. 1609–1621.

Moore, J.M., Howard, A.D., Umurhan, O.M., White, O.L., Schenk, P.M., Beyer, R.A., McKinnon, W.B., Spencer, J.R., Singer, K.N., Grundy, W.M., Earle, A.M., Schmitt, B.,

Protopapa, S., Nimmo, F., Cruikshank, D.P., Hinson, D.P., Young, L.A., Stern, S.A., Weaver, H.A., Olkin, C.B., Ennico, K., Collins, G., Bertrand, T., Forget, F., Scipioni, F., 2018. Bladed terrain on Pluto: Possible origins and evolution. Icarus 300, 129–144. doi:10.1016/j.icarus.2017.08.031.

Moore, J.M., McKinnon, W.B., Spencer, J.R., Howard, A.D., Schenk, P.M., Beyer, R.A., Nimmo, F., Singer, K.N., Umurhan, O.M., White, O.L., Stern, S.A., Ennico, K., Olkin, C.B., Weaver, H.A., Young, L.A., Binzel, R.P., Buie, M.W., Buratti, B.J., Cheng, A.F., Cruikshank, D.P., Grundy, W.M., Linscott, I.R., et al., 2016. The geology of Pluto and Charon through the eyes of New Horizons. Science 351, 1284–1293. doi:10.1126/science.aad7055.

Okorie, A., Makrogiannis, S., 2019. Region-based image registration for remote sensing imagery. Computer Vision and Image Understanding 189, 102825. doi:10.1016/j.cviu.2019.102825.

Pedregosa, F., Varoquaux, G., Gramfort, A., Michel, V., Thirion, B., Grisel, O., Blondel, M., Prettenhofer, P., Weiss, R., Dubourg, V., et al., 2011. Scikit-learn: Machine learning in Python. Journal of Machine Learning Research 12, 2825–2830.

Pluim, J.P.W., Maintz, J.B.A., Viergever, M.A., 2003. Mutual-information-based registration of medical images: a survey. IEEE transactions on medical imaging 22, 986–1004.

Protopapa, S., Grundy, W., Reuter, D., Hamilton, D., Ore, C.D., Cook, J., Cruikshank, D., Schmitt, B., Philippe, S., Quirico, E., Binzel, R., Earle, A., Ennico, K., Howett, C., Lunsford, A., Olkin, C., Parker, A., Singer, K., Stern, A., Verbiscer, A., Weaver, H., Young, L., 2017. Pluto's global surface composition through pixel-by-pixel Hapke modeling of New Horizons Ralph/LEISA data. Icarus 287, 218–228. doi:10.1016/j.icarus.2016.11.028.

Reuter, D.C., Stern, S.A., Scherrer, J., Jennings, D.E., Baer, J.W., Hanley, J., Hardaway, L., Lunsford, A., McMuldroch, S., Moore, J., Olkin, C., Parizek, R., Reitsma, H., Sabatke, D., Spencer, J., Stone, J., Throop, H., Cleve, J.V., Weigle, G.E., Young, L.A., 2008. Ralph: A Visible/Infrared Imager for the New Horizons Pluto/Kuiper Belt Mission. Space Science Reviews 140, 129–154. doi:10.1007/s11214-008-9375-7.

Schenk, P.M., Beyer, R.A., McKinnon, W.B., Moore, J.M., Spencer, J.R., White, O.L., Singer, K., Nimmo, F., Thomason, C., Lauer, T.R., Robbins, S., Umurhan, O.M., Grundy, W.M., Stern, S.A., Weaver, H.A., Young, L.A., Smith, K.E., Olkin, C., 2018. Basins, fractures and volcanoes: Global cartography and topography of Pluto from New Horizons. Icarus 314, 400–433. doi:10.1016/j.icarus.2018.06.008.

Schmitt, B., Philippe, S., Grundy, W.M., Reuter, D.C., Côte, R., Quirico, E., Protopapa, S., Young, L.A., Binzel, R.P., Cook, J.C., et al., 2017. Physical state and distribution of materials at the surface of Pluto from New Horizons LEISA imaging spectrometer. Icarus 287, 229–260.

Schroeder, W., Ng, L., Cates, J., 2003. The ITK software guide.

Stern, S.A., Buie, M.W., Trafton, L.M., 1997. HST high-resolution images and maps of pluto. The Astronomical Journal 113, 827. doi:10.1086/118304.

White, O.L., Moore, J.M., McKinnon, W.B., Spencer, J.R., Howard, A.D., Schenk, P.M., Beyer, R.A., Nimmo, F., Singer, K.N., Umurhan, O.M., Stern, S.A., Ennico, K., Olkin, C.B., Weaver, H.A., Young, L.A., Cheng, A.F., Bertrand, T., Binzel, R.P., Earle, A.M., Grundy, W.M., Lauer, T.R., Protopapa, S., Robbins, S.J., Schmitt, B., 2017. Geological mapping of Sputnik Planitia on Pluto. Icarus 287, 261–286. doi:10.1016/j.icarus.2017.01.011.

Zitova, B., Flusser, J., 2003. Image registration methods: a survey. Image and vision computing 21, 977–1000.

Appendix A. Additional LEISA maps

This section contains two additional registered composition maps (the weak-band CH_4 ice band depth map and the CH_4 band position index map) referred to in 3.2 and the analysis, as well as the principal four maps in orthographic projection.

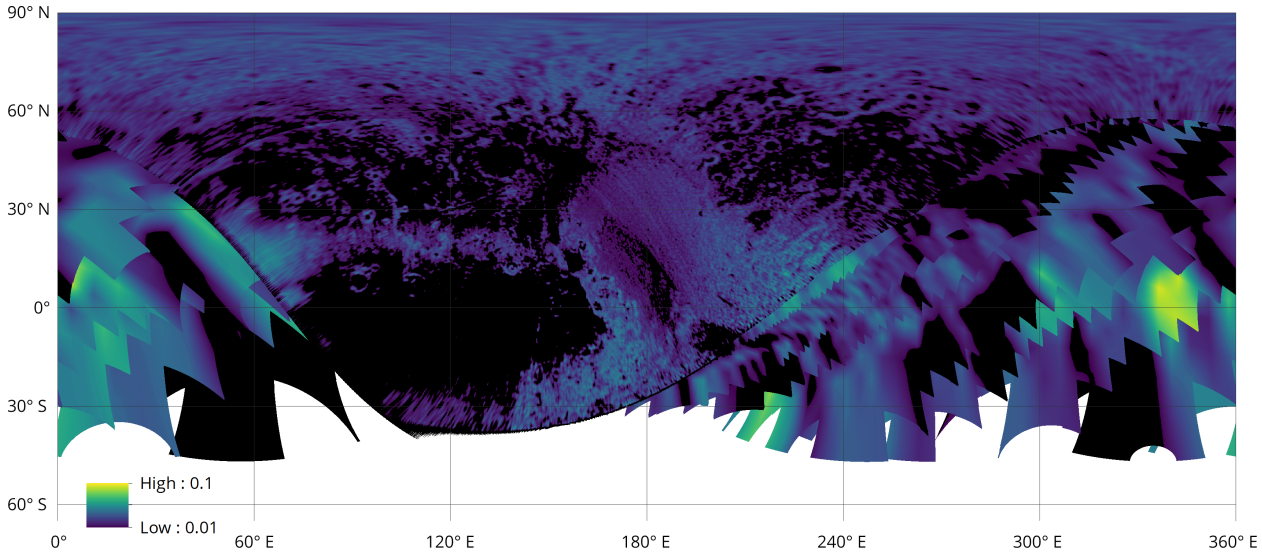

Figure A.1: Global registered CH_4 map of Pluto (1.95 μm integrated band depth).

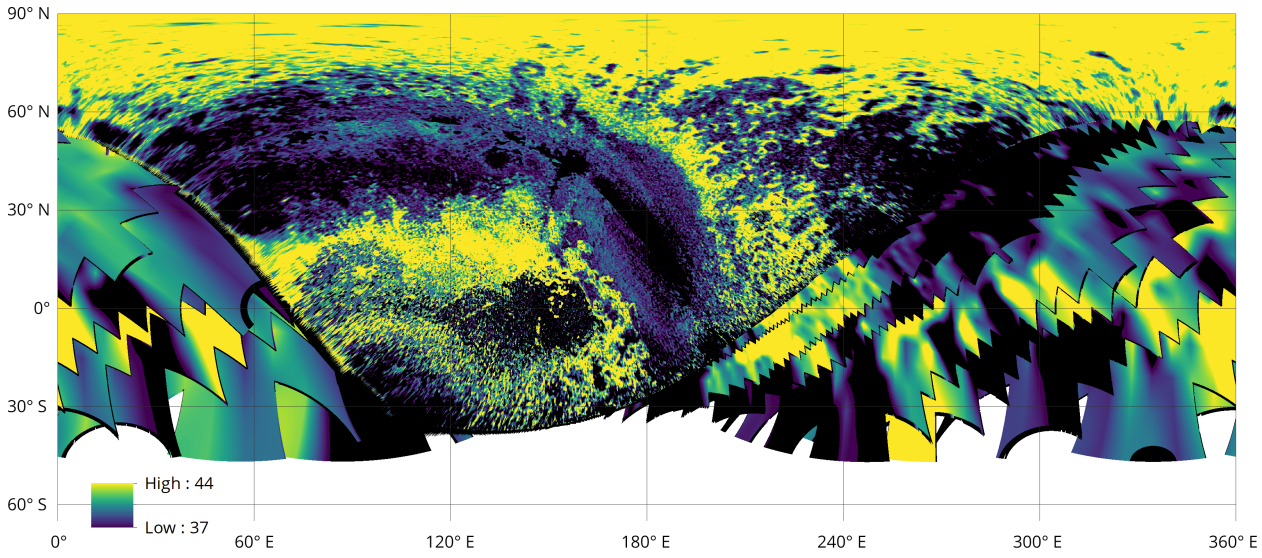

Figure A.2: Global registered CH_4 band position index (CH_4 state index) map of Pluto. The lower index limit is at a value of 36.5.

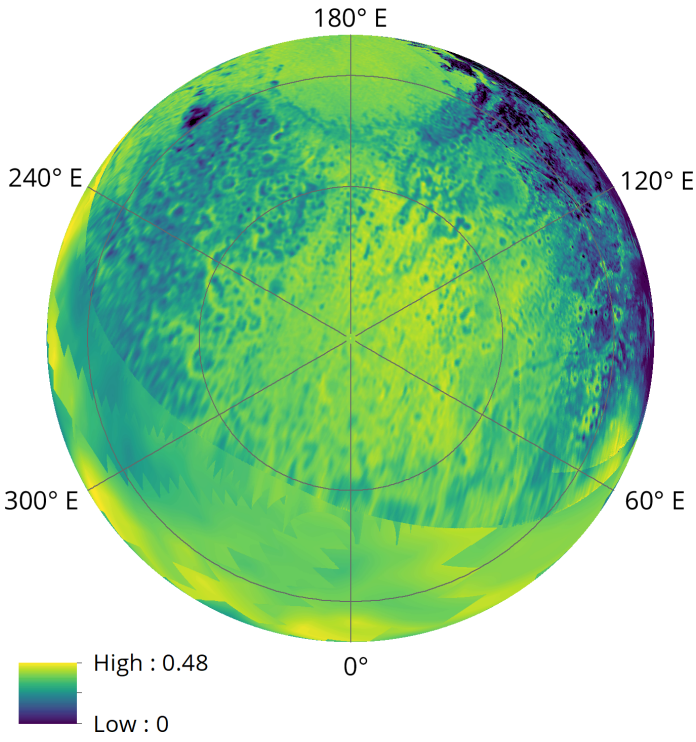

(a) Global registered CH_4 1.7-μm integrated band depth map of Pluto.

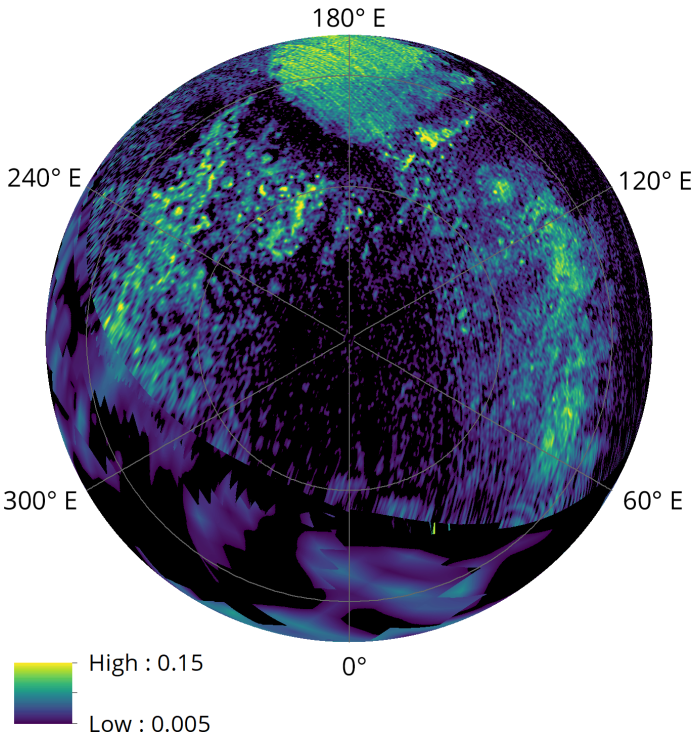

(b) Global registered N_2 2.15-μm band depth map of Pluto. The detection limit is at 0.005.

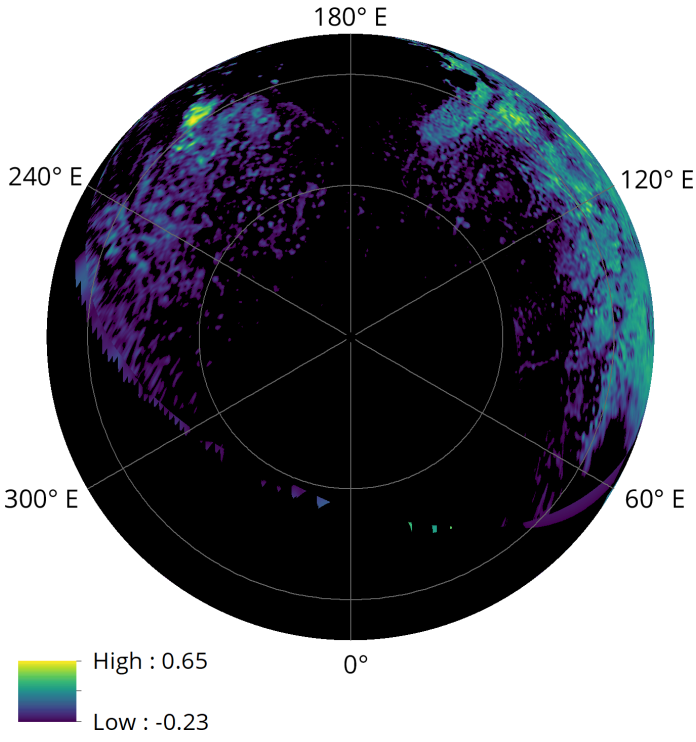

(c) Global registered H_2O spectral index map of Pluto. The detection limit is at -0.23.

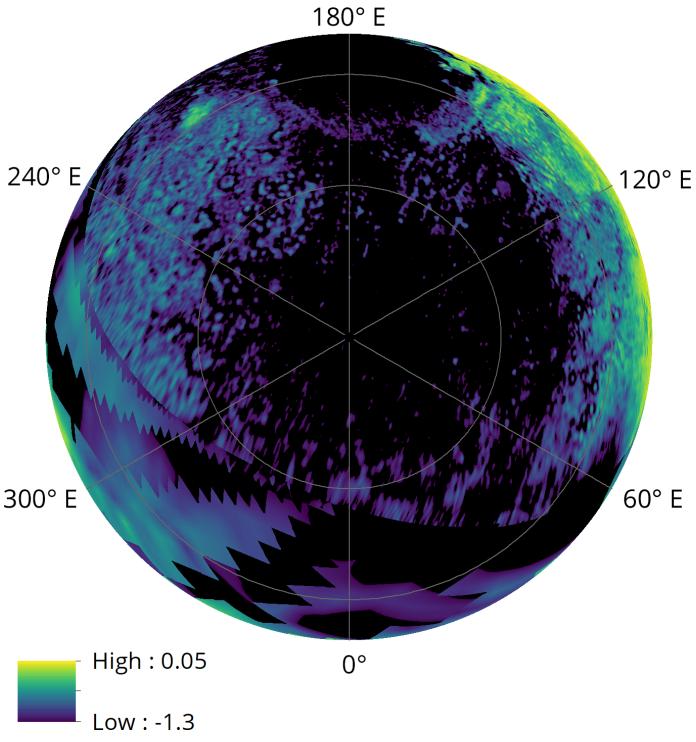

(d) Red material spectral index map of Pluto. The detection limit is at -1.3.

Figure A.3: Registered global LEISA maps in north polar orthographic projection.

Appendix B. Additional 2D correlation plots

This section contains 2D correlation plots between the LEISA datasets and the digital elevation map, for further information concerning which datasets correlate to altitude as referenced in section 4.3.

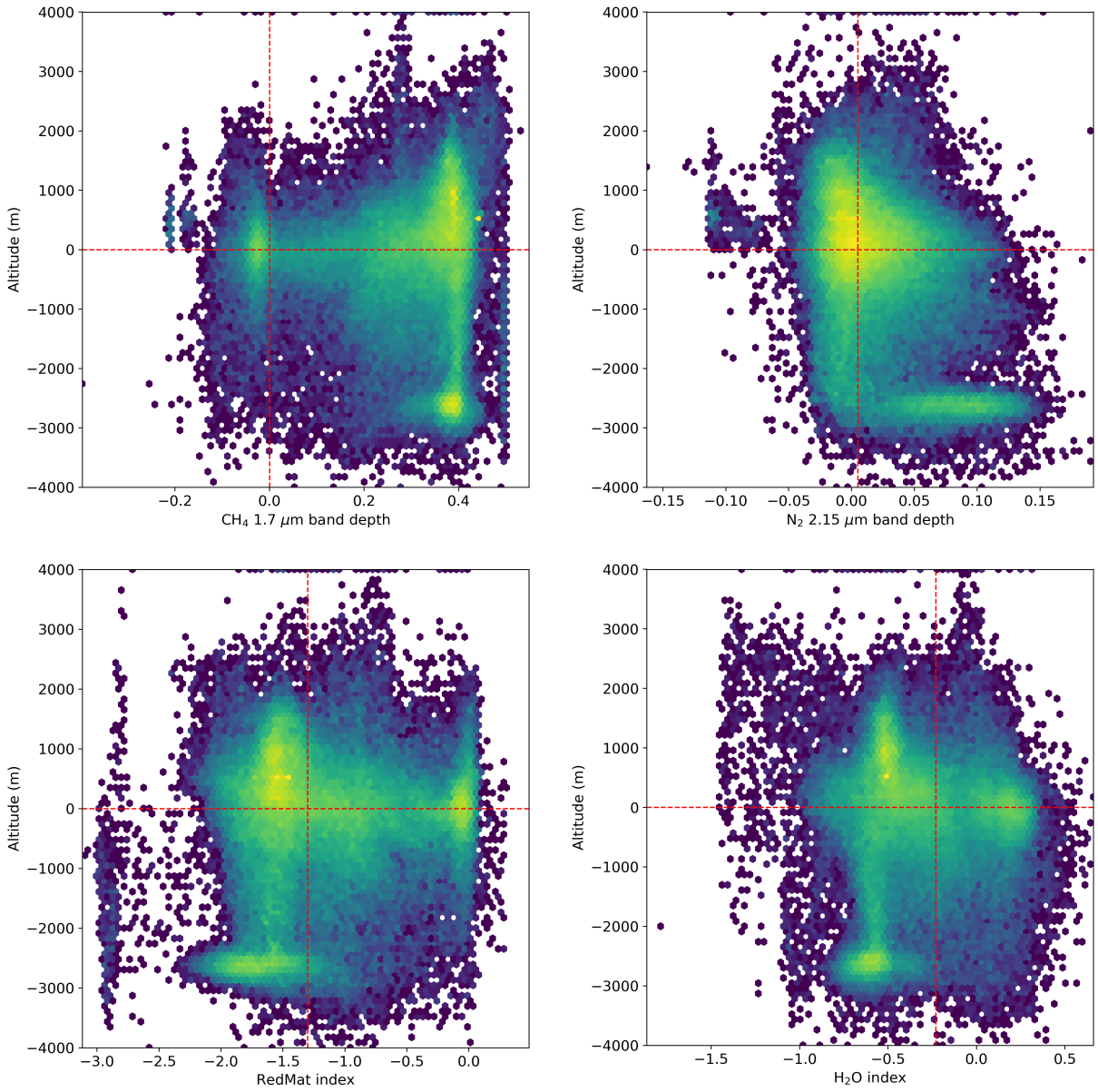

Figure B.4: Hexagonal bin plots showing correlations between different LEISA maps and the digital elevation map. The detection thresholds for each map are marked with a red dotted line.

Appendix C. Correlations as a function of latitude and longitude

This section contains latitude- and longitude-based correlation plots of each dataset pair analysed, allowing further study of how correlations between datasets vary with location.

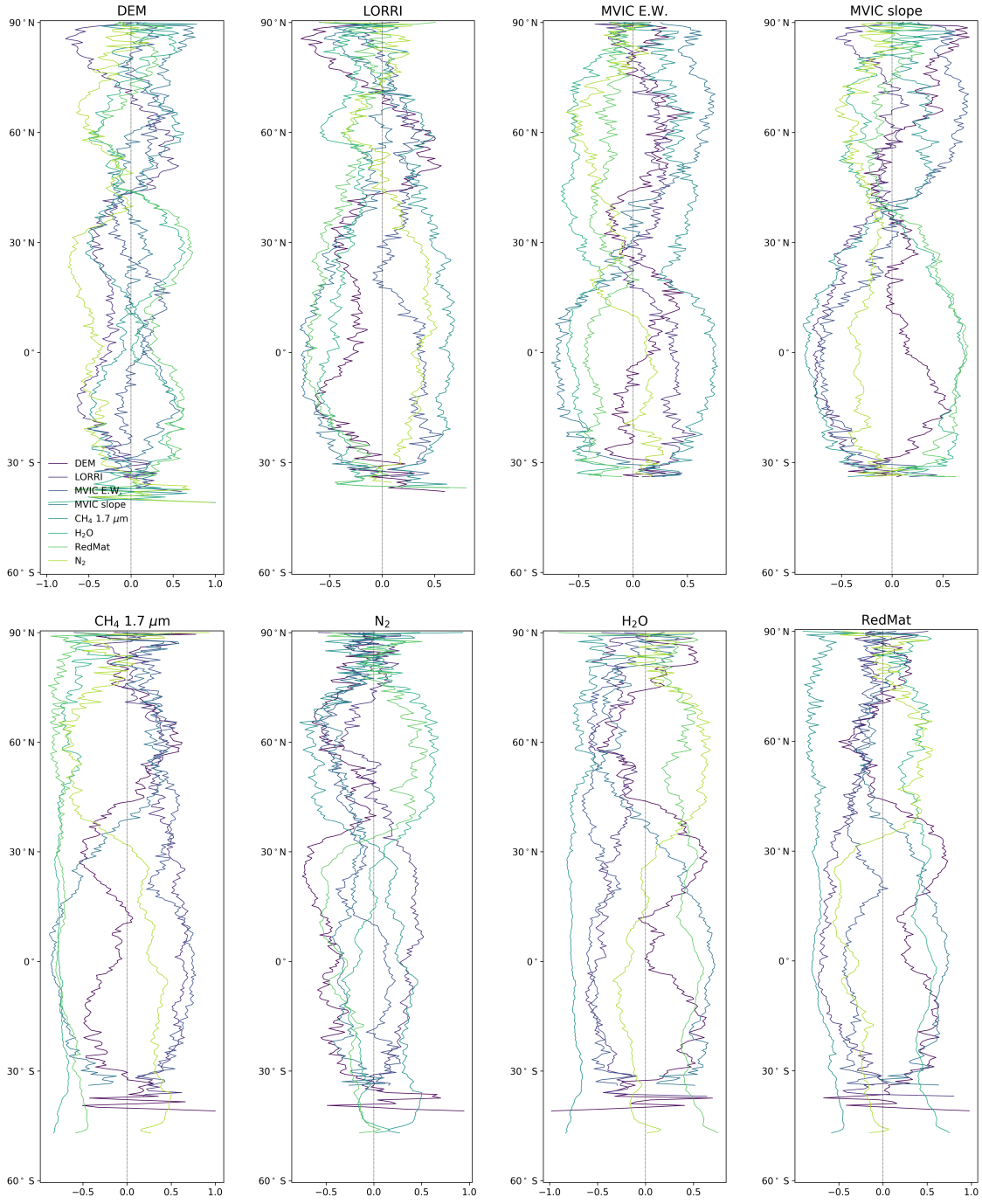

Figure C.5: Correlations between the datasets used as a function of latitude, grouped by LEISA datasets. For each pair of datasets, the Pearson correlation coefficient is calculated for each row of data points, corresponding to a range of 1.7 degrees of latitude.

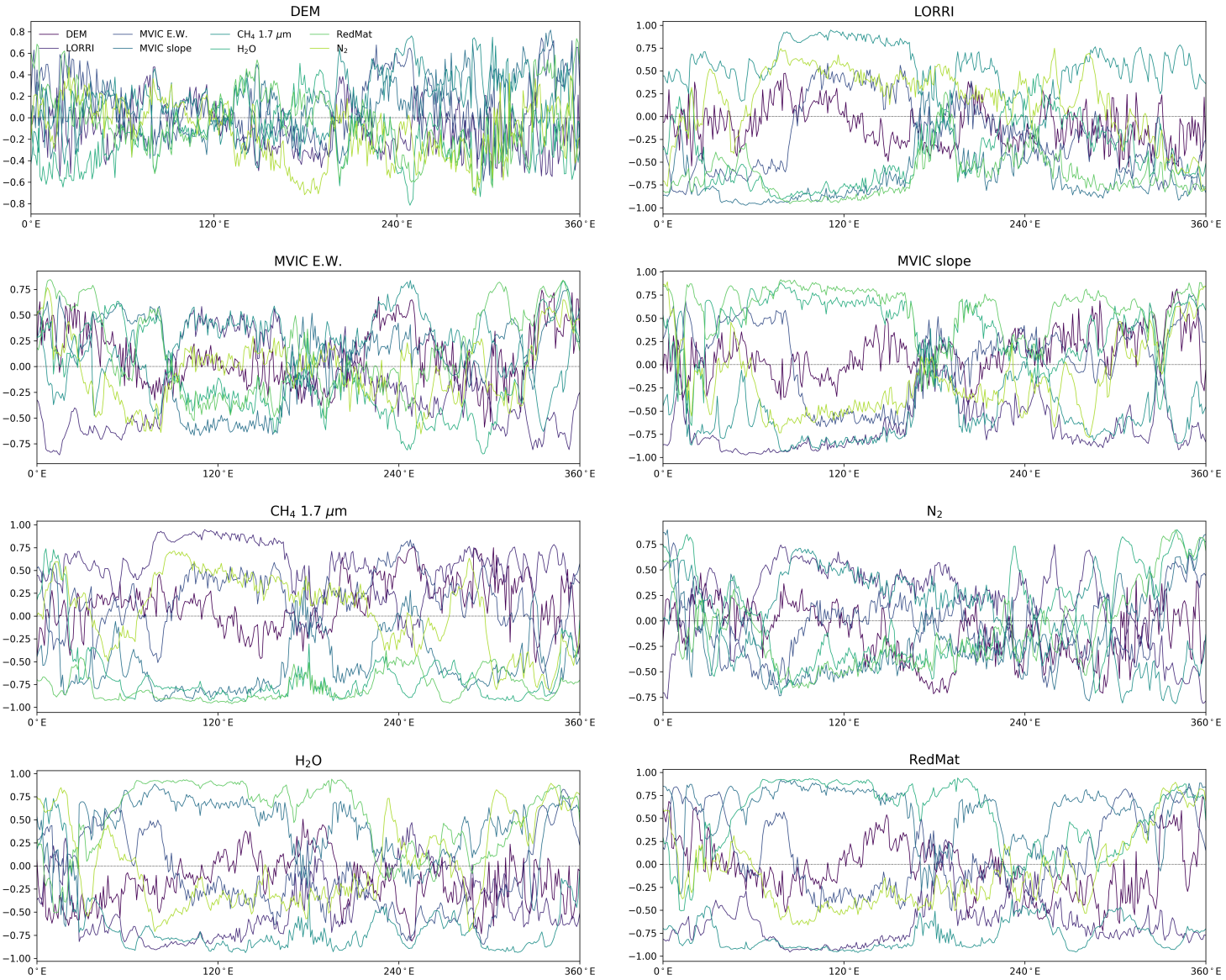

Figure C.6: Correlations between the datasets used as a function of longitude,grouped by LEISA datasets. For each pair of datasets, the Pearson correlation coefficient is calculated for each row of data points, corresponding to a range of 0.65 degrees of longitude. The calculation is weighted to compensate for latitude-based distortion due to the cylindrical projection.